THESIS FOR THE DEGREE OF LICENTIATE OF ENGINEERING

Modelling and Mitigation of Torque Ripple in Permanent Magnet Synchronous Machines

Qixuan Chenwei Wang

Department of Electrical Engineering
Chalmers University of Technology
Gothenburg, Sweden, 2026

Modelling and Mitigation of Torque Ripple in Permanent Magnet Synchronous Machines

Qixuan Chenwei Wang

Acknowledgements, dedications, and similar personal statements in this thesis, reflect the author's own views.

Department of Electrical Engineering
Chalmers University of Technology
SE-412 96 Gothenburg, Sweden
Phone: +46 (0)31 772 1000

Printed by Chalmers Digital Printing
Gothenburg, Sweden, May 2026

Modelling and Mitigation of Torque Ripple in Permanent Magnet Synchronous Machines

Qixuan Chenwei Wang
Department of Electrical Engineering
Chalmers University of Technology

Abstract

Electrical machines as the key components of EVs, provide the torque for the powertrain and determine the dynamic performance. Nevertheless, this is accompanied by torque ripple and the electromagnetic excitation of noise, vibration, and harshness (NVH). To minimize the torque ripple without hardware modification, the control-oriented approach is the focus in this study.

This study starts from a design and analysis process, which establish the base of the analysis and mitigation of torque ripple. In this process, a reference permanent magnet synchronous machine (PMSM) is designed and its characteristics including efficiency map, torque, flux linkage, back-EMF, radial flux and force density, core loss, as well as reduced order model (ROM) are compared.

Moving towards torque ripple mitigation, to develop the control-oriented approach, several designed-oriented approaches including skewing, notching and optimization are investigated first and set as the reference. To reduce manufacturing cost and increase flexibility, harmonic current injection method is investigated. To extract and inject harmonic components, the stochastic gradient descent algorithm and phase-locked loop are implemented to identify the amplitude and phase of the torque ripple, respectively. The results show that the control-oriented method can effectively reduce the torque ripple, and reveal the potential of this method, which is competitive with the design-oriented method but without hardware modification.

To further analyze the torque ripple when the PMSM coupled with the inverter, a circuit-based PMSM model needs to be implemented. In this study, a time-efficient spatial harmonics modelling method of a PMSM in polar coordinates is proposed to reduce the flux mapping time. The results show a significant mapping time reduction utilizing the proposed method, and it captures the saturation and spatial harmonics while maintains high fidelity.

Keywords: Permanent magnet synchronous machine, torque ripple, noise, vibration, and harshness, finite element method, spatial harmonics, harmonic injection.

To my family.

Contents

Acknowledgments

First of all, I would like to thank my main supervisor, Prof. Torbjörn Thiringer, and my co-supervisor, Dr. Joachim Härsjö, for their support, guidance, and encouragement throughout my studies. Their expertise and insightful feedback have shaped not only this work but also the way I think about problems. I am deeply grateful for the opportunity to learn from them.

I would like to express my gratitude to the Swedish Electromobility Center for providing financial support. I would also like to thank our industrial partners, Volvo Cars, Alstom, and Aurobay, as well as the colleagues in the reference group for sharing practical experience and advice.

A special thanks goes to my colleagues and friends at Chalmers. The discussions and assistance in the office and lab, the conversations during fika and lunch, made this journey not only productive but also enjoyable.

Finally, I want to thank my family for their unwavering support and encouragement throughout these years. Their patience and understanding, particularly during the more demanding stages of this work, are very much appreciated.

Qixuan Chenwei Wang
Göteborg, Sweden
May, 2026

Acronyms

EV:	Electric Vehicle
PM:	Permanent Magnet
PMSM:	Permanent Magnet Synchronous Machine
NVH:	Noise, Vibration, and Harshness
FEA:	Finite Element Analysis
FEM:	Finite Element Method
MMF:	Magnetomotive Force
EMF:	Electromotive Force
PWM:	Pulse Width Modulation
FFT:	Fast Fourier Transform
SRF:	Synchronous Reference Frame
LUT:	Lookup Table
ROM:	Reduced Order Model
HCI:	Harmonic Current Injection
SGD:	Stochastic Gradient Descent

CHAPTER 1

Introduction

1.1 Problem Background

With the global transition toward sustainable transportation, the share of electric vehicles (EVs) in the vehicle fleet is increasing, contributing to a growing demand for electrical machines. Among the various electrical machine topologies for EV propulsion systems, permanent magnet synchronous machines (PMSMs) have emerged as the primary choice. PMSMs are characterized by high efficiency and high power density, making them well-suited to the usage in an automotive application.

However, PMSMs suffer from torque ripple and radial electromagnetic force, making them a possible factor that leads to noise, vibration, and harshness (NVH) problems [1]. Achieving silent and smooth operation is crucial for EVs to meet customers' expectations and establish the cornerstone of brand perception. With the increasing demand for driving comfort, NVH problems present new challenges. The NVH qualification originated in the automotive industry to address the rumbling, knocking, and grinding generated by combustion engines. Unlike internal combustion engine (ICE) vehicles, EVs operate in a relatively silent environment. This exposes noise and vibration

phenomena that were previously not audible, elevating the NVH problem to one of the most critical concerns in terms of both passenger comfort and reliability in the automotive industry.

In a PMSM drive system, electromagnetic, mechanical, and aerodynamic sources all participate in generating noise and vibration, making systematic characterization and mitigation a substantial challenge.

Electromagnetic forces including radial and tangential Maxwell stress forces are generated by the interaction between the rotating magnetic field produced by the stator windings and the permanent magnets. The tangential force acting on the stator teeth produces torque, while the radial force produces vibration. These forces are spatially and temporally periodic, and when their spatial orders coincide with the natural mode shapes of the stator structure, resonances can be excited, producing audible tonal noise and structural vibrations that can be transmitted to the vehicle cabin through the housing, gears, and drivetrain. The frequencies of these excitations are directly related to the number of stator slots, pole pairs, and the fundamental electrical frequency, which means they shift with motor speed and produce characteristic harmonic orders that sweep across the audible range during acceleration or braking.

Torque ripple is a related but distinct electromagnetic NVH mechanism. The inherent torque ripple, known as cogging torque, is caused by the magnetic reluctance variation. Without current excitation, the rotor tend to align with positions of minimum magnetic reluctance, and this introduces a periodic disturbance at a frequency determined by the least common multiple of the slot and pole numbers. Superimposed on this is torque ripple, resulting from the harmonic components of the back-EMF waveform and the current harmonics produced by PWM-driven inverters. These ripple components are directly transmitted through the drivetrain as torsional excitations and are perceived as fluctuations in vehicle speed or as low-frequency vibration through the chassis, particularly at low vehicle speeds during creep or light acceleration.

The power converter that drives the PMSM introduces additional NVH excitations. PWM switching at the inverter generates voltage harmonics at multiples of the switching frequency and their sidebands, which drive corresponding current harmonics in the stator windings. These current harmonics produce flux density components that generate sideband electromagnetic forces on the stator teeth at frequencies that may cause structural resonances of the machine. Blanking time further increases the current distortion and

torque ripple problem.

1.2 Previous Work

FEM comparison: In order to analyze the electromagnetic performance of an electrical machine, it is crucial to select a suitable software before proceeding with modelling and analyzing. Some comparisons have been made between commercial software as well as open source software with the consideration of accuracy, ease of use and solving speed which are essential properties. In [2], a 1.1kW 4-pole induction machine was analyzed using Ansoft Maxwell (now Ansys Electronics Desktop), Cedrat Preflux (now Altair Flux), Ansys Multiphysics and Ansys Workbench. The magnetic flux line, magnetic flux density distribution and torque were compared between these FEM software. Besides, both advantages and disadvantages of these software were discussed regarding the accuracy and ease of use. In [3], [4], a 5kW, 4-pole induction machine was compared between commercial and open-source software with two-dimensional (2-D) models and a multislice model (2.5-D). The core losses were mainly concerned in this study and the results of open-source software showed a good agreement with the commercial one and measured values. In [5], a ferrite magnet assisted synchronous reluctance machine (FMaSynRM) was investigated and its simulation results were compared both at no load and load condition between the open-source software Elmer and the commercial software Altair Flux. At no load condition, two software gave similar results regarding terminal voltage, flux linkage, flux density and flux line distributions. Furthermore, maximum discrepancy was less than 2.5% for cogging torque, while at load condition, a 5.5% error existed in average electromagnetic torque due to different solver and mesh settings. In [6], a 30-slot/4-pole synchronous reluctance motor (SynRM) was compared using the commercial software Altair Flux and JMAG Designer as well as the open-source platform FEMM. However, the results of the three software were not similar, and lower average torque was given in the open-source software, possibly due to the lower quality mesh in the airgap.

In these studies, only a part of the electromagnetic performance was investigated, and PMSM was not the main focus. Therefore, further investigation needs to be done.

Spatial harmonics model: Several modelling methods have been pro-

posed to obtain high-fidelity PMSM models with the nonlinear characteristic. In [7], to capture the effects associated with the electromagnetic behavior of the machines, including magnetic saturation, spatial harmonics, and the iron loss effect, a model is proposed and it has been validated by both FEM and experiments. In [8], a nonlinear model of an electrically excited synchronous machine in the abc-reference frame is developed using N-dimensional lookup tables. Generating models in the abc-reference frame will have one more dimension data compared to the dq-reference frame, which will increase the computational burden. In [9] and [10], different fidelity PMSM models including inductance-based, flux-based and spatial flux-based models are compared regarding the impact of model fidelity on performance analysis and control. Different nonlinear modeling methods of asymmetrical dual three-phase interior permanent magnet synchronous motors are compared in [11] as well. The current-based method, which requires the computation of incremental and apparent inductance matrices to establish current-flux linkage relations, shows more complexity compared to the flux linkage-based method regarding data preparation and post-processing. In [12], a novel modeling method based on a stator winding flux linkage table for PMSM is presented. The steady-state phase A current and voltage are measured, and the flux linkage of all test points are calculated to build the PMSM model. In [13], a model of an IPMSM considering saturation, cross coupling, spatial harmonics, and temperature effects is derived using Co-energy method. In this work, some assumptions are made such as no core losses and constant energy stored in the magnet, which may lead to the discrepancies.

However, the mapping time of a PMSM model was not the main focus in the studies mentioned above, and only a part of the electromagnetic performance were investigated.

Torque ripple mitigation: To improve NVH performance, extensive research has been done to mitigate torque ripple. Torque ripple mitigation can be generally divided into two categories: design-oriented and control-oriented approaches [14].

Design-based methods focus on modifying the stator and rotor design topologies using techniques such as slot/pole combination, skewing, notching, etc. In [15], an optimal magnet-skewing method based on frequency-domain is proposed. It can eliminate arbitrary multiple harmonics in the back EMF. However, the average torque and overall efficiency are compromised compared

to the conventional skewing method. In [16], a rotor design with axial pole shaping is proposed to reduce torque ripple. The design uses a number of rotor segments with different pole arcs on the rotor surface to create a specific flux density pattern along the axial direction, subsequently achieving a low torque ripple with minimum average torque reduction. In [17], a piecewise inverse cosine function is applied to modify the rotor shape for making the air-gap flux density distribution sinusoidal under no-load conditions, which can reduce the torque ripple.

For control-based methods, advanced control algorithms including filter and harmonics injection are applied to minimize torque ripple without modifying the motor design, which makes it a better choice considering manufacturability and flexibility. In [18], a proportional-integral-resonant (PIR) controller was introduced for the speed loop to produce an accurate current reference signal for the inverter, and further mitigate the torque ripple. In [19], a torque ripple model based on the general airgap field modulation theory is proposed. With the extracted coefficients from FEA, the phase and amplitude of the injected harmonic current are determined to minimize the torque ripple.

From the studies mentioned above, it can be seen that the manufacturing cost and the tradeoff between torque ripple and average torque are inevitable using the design-oriented approach. The control-oriented approach is promising because it is applicable to existing machine design without hardware modification. Therefore, to mitigate torque ripple while maintaining the average torque, the control-oriented method is necessay to be investigated.

1.3 Purpose

The purpose of this thesis is to develop a torque ripple mitigation method without hardware modification. The widely used design-oriented mitigation methods require hardware modifications, which leads to average torque loss and higher manufacturing cost. Therefore, this study takes design-oriented as a reference and compare with the developed control-oriented method. In order to conduct this comparison, a needed step is to also make a hardware modification effort.

1.4 Contributions

The main contributions of this thesis can be summarized as the following parts,

FEM comparison: A design and analysis process with parallel tracks is proposed for the purpose of comparing PMSM electromagnetic performance and different FEM software solving performance. Quantification of the electromagnetic performance including torque, back-EMF, flux linkage, radial flux density, core loss, as well as efficiency map for three FEM software has been done. The discrepancy of flux linkage under different input current with different phase advance angles has been quantified. Reduced order models incorporated in the software tracks has been generated and their performances have been established.

Spatial harmonics model: The proposed modelling method takes the operating region of traction PMSMs into consideration. The mapping time of the proposed method is reduced compared to that of the Cartesian method. The validity is confirmed and the results between the FEM simulation and the proposed model have been compared. The nonlinear FEM solving time in JMAG has been measured.

Torque ripple mitigation: The widely used mitigation methods including skewing, auxiliary notch and geometry optimization are investigated and discussed. A gradient descent based harmonic current injection is introduced and implemented. The reduced order model and PWM excitation are taken into account. The DOFs in the stochastic gradient descent method are compared.

1.5 Thesis Outline

The outline of this thesis is listed as follows

Chapter 2, introduces the fundamental theories including electromagnetic force, torque, and core loss calculation methods in FEM software. Based on that, the causes and mitigation methods of torque ripple and vibro-accoustics are investigated.

Chapter 3, details the case setups including two reference PMSMs, and their

design geometries, dimensions, and parameters.

Chapter 4, proposes a multi-stage design and analysis process with two parallel software tracks. This chapter utilizes and compares different FEM software for different stages including the initial design stage, analysis stage, and system-level stage.

Chapter 5, presents a computationally efficient method for building a circuit-based PMSM model. This chapter outlines the steps of circuit model implementation, flux maps generation, and inversion of flux maps.

Chapter 6, focuses on design-oriented torque ripple mitigation methods. Design-oriented mitigation methods including skewing, notching, and geometry optimization are investigated.

Chapter 7, focuses on control-oriented torque ripple mitigation methods to avoid hardware modification. First, the harmonic current injection method is investigated, and its effectiveness is validated. Furthermore, to adaptively mitigate the torque ripple, a stochastic gradient descent based method is implemented, and its performance is validated.

1.6 List of Publication

[1] **Qixuan C. Wang**, Torbjörn Thiringer and Joachim Härsjö. "Multi-Stage Design and Analysis of a Permanent Magnet Synchronous Machine with Parallel Comparison Tracks", 2025 IEEE International Electric Machines & Drives Conference (IEMDC), Houston, TX, USA, 2025, pp. 1051-1056.

[2] **Qixuan C. Wang**, Torbjörn Thiringer and Joachim Härsjö. "Time Efficient Nonlinear Spatial Harmonics Modelling Method of Permanent Magnet Synchronous Machines in Polar Coordinates", 2025 IEEE Transportation Electrification Conference and Expo, Asia-Pacific (ITEC Asia-Pacific), Singapore, 2025, pp. 1-6.

[3] **Qixuan C. Wang**, Torbjörn Thiringer and Joachim Härsjö. "Stochastic

Gradient Descent Based Torque Ripple Mitigation of Permanent Magnet Synchronous Machines: A Comparative Study", 2026 International Conference on Electrical Machines (ICEM), Funchal, Portugal, 2026.

CHAPTER 2

Theory of Torque Ripple and NVH Reduction

2.1 FEA Calculation Methods for Electromagnetic Performance Quantities

Finite Element Method (FEM) is a numerical method for electrical machine design and analysis. Electrical machines involve complex geometries, nonlinear materials, and coupled physical effects. Compared to analytical solutions, FEM can solve electromagnetic field equations numerically with high accuracy.

Therefore, FEM software are the primary option to capture torque ripple in PMSMs. This section focuses on electromagnetic calculation methods of different electromagnetic performance quantities in FEM software.

2.1.1 Electromagnetic Torque

There are several methods to analyze electromagnetic torque, and each suited to different problem types and accuracy requirements. The choice often depends on the geometry and mesh quality, etc.

Maxwell Stress Tensor

The Maxwell stress tensor (MST) is often employed in the calculation of forces and torque

$$T_e = \frac{r^2 L}{\mu_0} \int_0^{2\pi} B_r B_t \, d\theta \tag{2.1}$$

where μ_0 is air permeability, L is stack length, r is the radius of the chosen contour between stator inner radius and rotor outer radius, B_r and B_t are the radial and tangential components of the flux density.

MST features quick computation but it requires a fine mesh at the chosen contour. To improve its accuracy, different variants are proposed.

Arkkio's Method

The Arkkio method is a variant of MST. Instead of integrating over a single contour, it averages over the entire air gap volume

$$T_e = \frac{l}{\mu_0 (r_{out} - r_{in})} \int_{r_{in}}^{r_{out}} \int_0^{2\pi} r B_r B_t \, d\theta dr \tag{2.2}$$

where r_{in} and r_{out} are the inner and outer radii of the air gap region.

Compared to MST, the Arkkio method is less sensitive to local numerical inaccuracies, and reduces noise caused by mesh quality. [20] Therefore, the Arkkio method improves the torque calculation which is especially important for torque ripple analysis.

Virtual Work

If a virtual rotor displacement is applied, torque can be considered as incremental work done by magnetic forces. Hence, unlike MST, the virtual work (VW) method computes torque as a function of rotor displacement while keeping flux linkage constant, and can be expressed as

$$T_e = \frac{\partial W(\psi, \theta)}{\partial \theta} \tag{2.3}$$

where W represents the stored energy as a function of flux linkage ψ and rotor displacement θ.

VW has high accuracy for saturation condition, and it is numerically robust to mesh quality compared to MST. However, it will increase computational burden.

Co-Energy

If the magnetic energy stored in the stator and rotor iron cores is assumed to be negligible, energy variation will only occur in the air-gap. Therefore, closely related to VW, the co-energy method computes torque from the co-energy while keeping current constant, can be expressed as

$$T_e = \frac{\partial W'(i,\theta)}{\partial \theta} \tag{2.4}$$

where W' represents the magnetic co-energy as a function of current i and rotor displacement θ.

For a non-saturated situation, the co-energy is equal to the stored energy, and (2.3) and (2.4) give identical results. The general relation between stored energy and co-energy is given by Legendre's transform as follows,

$$W(\psi,\theta) + W'(i,\theta) = \Psi i \tag{2.5}$$

2.1.2 Electromagnetic Force

To analyze the vibration in PMSMs, the electromagnetic force applied on the stator teeth needs to be investigated. Since torque is generated from electromagnetic force, the calculation methods of electromagnetic force are basically the same as discussed in the previous section.

To further clarify the source of vibration, the electromagnetic force can be further divided in to radial force and tangential force.

Radial Force

The radial force acts perpendicular to the air gap which is responsible for vibration. Based on the Maxwell stress tensor, the radial force density can be expressed as

$$f_r = \frac{1}{2\mu_0}(B_r^2 - B_t^2) \tag{2.6}$$

where f_r is the radial force density.

Accordingly, the radial force can be expressed as

$$F_r = \frac{rL}{2\mu_0}\int_0^{2\pi} (B_r^2 - B_t^2)\, d\theta \tag{2.7}$$

Tangential Force

The tangential force acts along the air-gap circumference which is responsible for torque production as well as torque ripple. Based on Maxwell stress tensor, the tangential force density can be expressed as

$$f_t = \frac{1}{\mu_0} B_r B_t \tag{2.8}$$

where f_t is the tangential component of force density, and B_r and B_t are the radial and tangential components of flux density, repectively.

Accordingly, the tangential force can be expressed as

$$F_t = \frac{rL}{\mu_0} \int_0^{2\pi} (B_r B_t)\, d\theta \tag{2.9}$$

2.1.3 Core Loss

Apart from torque and force, core loss is another key objective to evaluate the FEM models. The common core loss models in FEM software fall into empirical and physics-based models.

Steinmetz Model

The Steinmetz model is one of the classical empirical models and the original formula can be expressed as

$$P_{Steinmetz} = k f^{\alpha} B^{\beta} \tag{2.10}$$

where f is the frequency, B is the magnetic flux density, and k, α, β are the material-fitted coefficients.

In Motor-CAD, the modified Steinmetz model separates terms for hysteresis and eddy current losses, and can be expressed as

$$P_{Steinmetz} = k_h f B^{(\alpha+\beta \cdot B)} + 2\pi^2 k_{eddy} f^2 B^2 \tag{2.11}$$

where k_h is the hysteresis loss coefficient, k_e is the eddy current loss coefficient.

The empirical models feature fast estimation but less accurate.

Bertotti Model

Compared to empirical models, physics-based models separate core loss into physical components. The most widely used model in FEA software is the Bertotti model with three terms, which is given as

$$P_{Bertotti} = k_h f B^{\alpha} + k_{eddy} f^2 B^2 + k_{ex} f^{\frac{3}{2}} B^{\frac{3}{2}} \tag{2.12}$$

where k_{ex} is the excess loss coefficient.

In Ansys Maxwell, the hysteresis loss term in (2.12) is $k_h f B^2$ for earlier versions (2023R2 and before), and $k_h f B^Y$ for later versions (2024R1 and later).

In these loss models, since they are frequency-domain models, B is the maximum amplitude of the flux density. However, for non-sinusoidal waveforms, e.g., PWM excitation, time-domain models will be more suitable for inverter-fed drives. Therefore, when the instantaneous waveform is taken into account, dB/dt is used instead of the peak value of B.

2.2 Vibration and Noise

Vibration and noise in PMSMs is considered as a cause-and-effect chain, where vibration is a mechanical phenomenon and noise is its acoustic consequence. The excitation force acts on the stator teeth, then the stator and housing respond to the force as a mechanical system which causes the structural response i.e., vibration. The vibrating surface pumps pressure waves into the air-borne generating acoustic radiation i.e., noise.

2.2.1 Radial Electromagnetic Force

Radial electromagnetic force is the primary source of vibration and noise in PMSM. It acts on the stator teeth, cause the deformation of the stator yoke and vibration. The flux density in (2.6) is the product of the magnetomotive force (MMF) and the air-gap permeance:

$$B_r = F(\theta, t) \cdot \Lambda(\theta, t) \tag{2.13}$$

The MMF harmonics can be written as

$$F(\theta, t) = \sum_v F_v cos(vp\theta - v\omega t + \phi_v) \tag{2.14}$$

where v is the MMF harmonic order, p is the number of pole pairs.

The permeance harmonics can be written as

$$\Lambda(\theta) = \Lambda_0 + \sum \Lambda_\mu cos(\mu N_s, \theta) \tag{2.15}$$

where μ is the permeance harmonic order.

Multiplying MMF and permeance gives the spatial orders of flux density harmonics

$$f = \mu N_s \pm vp \tag{2.16}$$

2.2.2 Tangential Electromagnetic Force

The tangential electromagnetic force primarily generates electromagnetic torque and does not produce vibration directly. However, when it interacts with the radial electromagnetic force, despite the low amplitudes of the tangential electromagnetic forces, the corresponding contribution to the vibration in PMSMs can not be neglected.

The tangential electromagnetic force also involves in the cogging torque and torque ripple of PMSMs. According to the Maxwell stress tensor method, the EM torque produced by kth-order radial and tangential flux density harmonics can be expressed as

$$T_k(t) = \frac{r^2 \pi L}{\mu_0} B_r B_t cos[\theta_r(t) - \theta_t(t)] \tag{2.17}$$

2.2.3 Sideband Electromagnetic Force

For inverter-fed PMSMs, sideband current harmonic components will be introduced around the carrier frequency with pulse width modulation (PWM) excitation. The general PWM current harmonic frequencies can be expressed as

$$f_h = m \cdot f_{sw} \pm n \cdot f_1 \tag{2.18}$$

The sideband harmonic component will generate high frequency harmonic magnetic fields that become one of the main sources of high frequency electromagnetic vibration [21]. Therefore, the sideband electromagnetic forces are of particular importance for electromagnetic vibration analysis in PMSM drives.

2.3 Torque Ripple Mitigation

To improve NVH performance, extensive research has been done to mitigate torque ripple and vibro-acoustics. The mitigation methods can be generally divided into two categories: design-oriented and control-oriented approaches.

Design-based methods focus on modifying the stator and rotor design topologies using techniques such as slot/pole combination, skewing, notching, etc.

2.3.1 Skew

Skewing technology has been widely used for the minimization of torque ripple and cogging torque. It can be classified into slot skew and rotor skew depending on the purpose.

Based on the skew patterns, it can be further divided into continuous skew, step skew, and V-type skew. The different skew patterns are illustrated in Fig. 2.1.

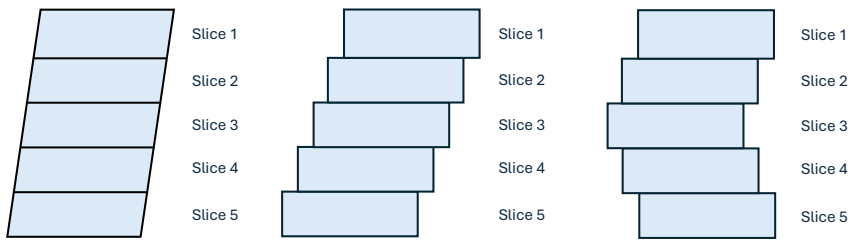

(a) Continuous skew **(b)** Step skew **(c)** V-type skew

Figure 2.1: Skew types

To mitigate the cogging torque, the angle of step skew can be calculated from the period of the cogging torque, the number of slots and poles [22],

$$\theta_{skew} = \frac{N-1}{N} \times \frac{2\pi}{LCM(N_s, N_p)} \tag{2.19}$$

and the angle of each step skew can be written as

$$\Delta\theta_{skew} = \frac{\theta_{skew}}{N-1} \tag{2.20}$$

where N is the number of slices, N_s is the number of slots, N_p is the number of poles, and LCM means the least common multiple.

However, from the previous analysis, cogging torque is one of the source of torque ripple. The $6k$ th torque ripple induced by harmonics is another dominant source, which means $(6k \pm 1)$th harmonics need to be mitigated. The skew angles for the $(6k \pm 1)$th harmonics are shown as

$$\theta_i = \frac{2\pi}{i * N_p} \tag{2.21}$$

where $i = 6k \pm 1$.

It can be seen that the skew angles in (2.20) and (2.21) are different. Therefore, the skew angle needs to be selected based on the dominant disturbance and the number of slices.

2.3.2 Auxiliary Notch

Auxiliary notches are another design modification method to mitigate torque ripple and vibro-acoustics, which can be divided into stator notching and rotor notching.

Compared to skewing, the auxiliary notches only modify the reluctance variation along the stator or rotor surface and does not change PM distributions, which means the notching employed on the surface can shift the phase of the cogging torque waveform and reduce its effects.

Therefore, torque ripple reduction can be achieved by a reasonable notching design. In general, the position and shape dimensions of the notches need to be determined.

2.3.3 Topology Optimization

Topology optimization is a comprehensive option to further minimize torque ripple and vibro-acoustics. The principle of this method is to utilize the multi-objective optimization method to find the optimal electromagnetic design of the PMSM [23].

In this method, the vibration or torque ripple generated by the PMSM which need to be reduced to improve the vibro-acoustic behavior, is defined as an objective function of the optimization algorithm. After the initial design and selection of the optimized objectives, the sensitivity analysis is implemented to evaluate the influence of each design parameter on different design objectives. Based on the sensitivity analysis, the design parameters with higher

correlation coefficients have priority. Various optimization algorithms, e.g. genetic algorithm or particle swarm optimization algorithm, can be applied to minimize the cost objective by modifying the selected design parameters in the FEM model. Finally, the candidate points can be chosen from the Pareto solutions for the multi-objective optimization.

2.3.4 Multiple Synchronous Reference Frame

Since the harmonic components rotate with different speed and angle, the fundamental and harmonic components can be regulated separately under multiple synchronous reference frame (MSRF). The illustration of the MSRF is shown in Fig. 2.22, and can be expressed as

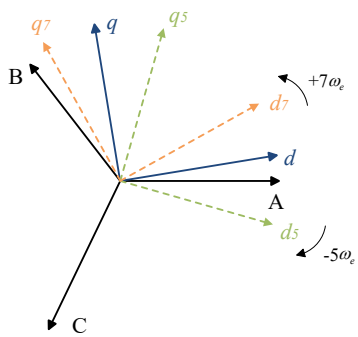

Figure 2.2: Multiple synchronous reference frame

$$\begin{bmatrix} i_d^n \\ i_q^n \end{bmatrix} = \begin{bmatrix} cos(n\theta) & sin(n\theta) \\ -sin(n\theta) & cos(n\theta) \end{bmatrix} \begin{bmatrix} i_\alpha \\ i_\beta \end{bmatrix} \tag{2.22}$$

Under the n-th order rotating frame, the n-th harmonic component becomes a DC component, and can be separated from other components by using a low pass filter (LPF). The inverse Park transform rotates the extracted DC component back to the $\alpha\beta$ frame, where it can be used as a reference or as an error signal for a feedforward injection term. However, the LPFs lead to significant delay and reduces the dynamic current response as well as the stability of control system.

2.3.5 Proportional-Integral-Resonant Controller

The proportional–integral–resonant (PIR) controller integrates a resonant component with the conventional PI controller. The PI term, as the main controller, determines the dynamic performance of the system and produces the DC control output. The resonant terms can deal with targeted frequencies and harmonic disturbances effectively. The transfer function of the PIR controller can be formulated as [18]

$$G_{PIR} = K_p + \frac{K_i}{s} + \frac{2K_{RC}\omega_c s}{s^2 + 2\omega_c s + \omega^2} \tag{2.23}$$

where ω is the angular frequency of the resonant controller, ω_c is the damping coefficient, K_p, K_i, K_{RC} are the proportional, integral, and resonant controller gains, respectively.

The resonant frequencies of the PIR controllers are based on the speed reference. In steady state, the resonant frequencies can coincide with the targeted frequencies, and the resonant terms can mitigate them effectively. However, in dynamic conditions, the controller input signals contain AC components, the output of resonant terms will increase and affect control performance [24].

CHAPTER 3

Case Setup

3.1 Overview

This chapter provide the specification of case setups including simulation settings and reference machine models. Detailed methodologies based on these setups are presented in the following chapters.

3.2 Case Setup 1

In case setup 1, a single-layer V-shape PMSM is selected as the reference machine. The number of slots and poles is 48/8, and single-layer distributed windings configuration is adopted for NVH performance. The machine geometry is shown in Fig. 3.1, and the detailed parameters and materials are listed in Table 3.1.

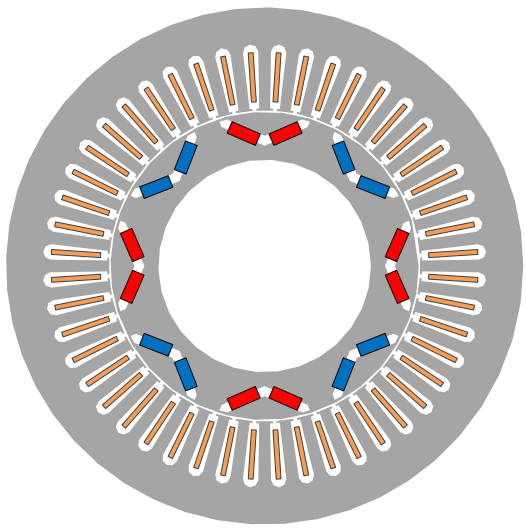

Figure 3.1: Topology of PMSM 1 with round wire

Table 3.1: Design Parameters of PMSM 1

Category	Parameter	Unit	Value
Power	Number of phase / slots / poles	-	3 / 48 / 8
	Peak power	kW	50
	Peak torque	Nm	400
	Peak Phase RMS Current	A	230
	DC-link Voltage	V	300
	Base speed	rpm	1200
	Maximum speed	rpm	6000
Dimension	Stator outer diameter	mm	269.24
	Stator inner diameter	mm	161.9
	Rotor outer diameter	mm	160.4
	Rotor inner diameter	mm	110.64
	Air-gap length	mm	0.75
	Lamination stack length	mm	83.82
	Stacking factor	-	0.95
Wiring	Type	-	Stranded
	Winding layers	-	1
	Number of turns	-	9
	Wire size	-	AWG 19
Material	Core material	-	M19-29G
	PM material	-	N36-Z20

3.3 Case Setup 2

In case setup 2, a double-layer V-shape PMSM is selected as the reference machine which is more related to the traction motor in current automotive industry. The number of slots and poles is 48/8, and equipped with 6-layer hairpin winding configuration. The design of geometry is shown in Fig. 3.2, and the detailed dimensions and materials are listed in Table 3.2.

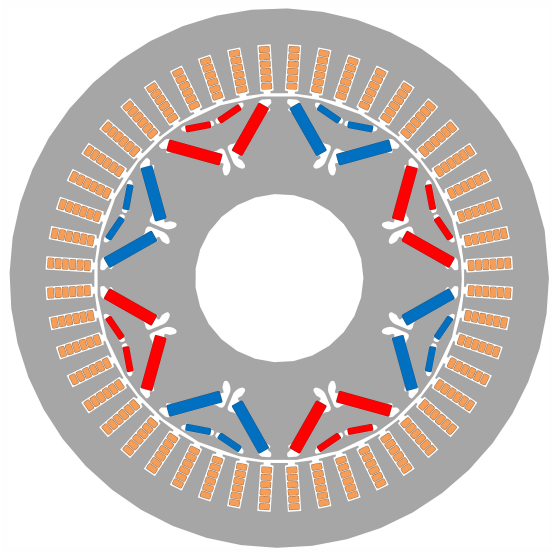

Figure 3.2: Topology of PMSM 2 with flat wire

Table 3.2: Design Parameters of PMSM 2

Category	Parameter	Unit	Value
Power	Number of phase / slots / poles	-	3 / 48 / 8
	Peak power	kW	135
	Peak torque	Nm	230
	Peak Phase RMS Current	A	380
	DC-link Voltage	V	350
	Base speed	rpm	5500
	Maximum speed	rpm	16000
Dimension	Stator outer diameter	mm	160
	Stator inner diameter	mm	109.8
	Rotor outer diameter	mm	108.2
	Rotor inner diameter	mm	50
	Air-gap length	mm	0.8
	Lamination stack length	mm	110
	Stacking factor	-	0.97
Wiring	Type	-	Hairpin
	Layers	-	6
	Wire size	-	3.12×1.88
Material	Core material	-	25SW1300
	PM material	-	N50UH

3.4 Simulation Settings

System Configuration

The system configuration is given as follows, the CPU is 12th Gen Intel(R) Core(TM) i7-12700 @2.10 GHz with 12 cores and 20 logical processors, the RAM is SK hynix 128GB DDR5 4800MHz 2Rx8 PC5 4800B.

Mesh Size Control

A fine mesh distribution is needed to reach the desired level of results. The mesh size control in order to ensure that the mesh qualities are basically consistent in the different FEM software, is given in Table 3.3. Moreover, to avoid the numerical error caused by movement [25], the mesh step is set synchronized with the displacement step, and the movement process is illustrated in Fig. 3.3.

Table 3.3: Mesh Size Control

Part	Maximum elements length
Stator core	2 mm
Rotor core	2 mm
Magnets	1 mm
Airgap layers	4

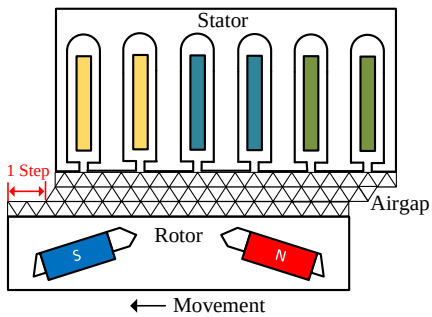

Figure 3.3: Movement process

Time Step

The time step is critical to get higher accuracy results, and can be expressed as

$$TimeStep = \frac{1}{Frequency} \frac{Cycle}{Points} \tag{3.1}$$

Higher time resolution will definitely provide highly accurate results, but it will also increase the computation burden. According to [26], the error depending on time resolution will converge and reach relatively high accuracy at 180 steps per electric period with fine mesh. Therefore, the number of points per electric period is set to 180 in this study for all software.

CHAPTER 4

Comparison of FEM Software

4.1 Overview

In this chapter, a design and analysis process with two parallel software tracks is utilized to design a PMSM and evaluate its electromagnetic performance. In this process, the reference PMSM of case setup 1 is selected and modelled and its characteristics including efficiency map, torque, flux linkage, back-EMF, radial flux and force density, core loss, as well as ROM are compared. In parallel tracks, different commercial FEM software from Ansys and JMAG are utilized as the tools.

4.2 Preliminaries

4.2.1 Design and Analysis Process

A design and analysis process with parallel tracks is outlined in Fig. 4.1. The design procedure assumed is to first use a 'quicker design tool' in a software series, Motor-CAD and JMAG Express are utilized as evaluation tools respectively. Here, depending on the complexity, each iteration can go quicker or

slower depending on the amount of calculations performed and results delivered. Motor-CAD has many features that can be extracted and thus require a bit longer time for each solution compared to JMAG Express. After having generated sufficient amount of machine design points, it is assumed that response surfaces (meta models) are created and an optimization tool is utilized, for instance Ansys optiSLang.

Once the initial design parameters are determined, the analysis of detailed electromagnetic performance needs to be carried out. Then, it is assumed that 10 possible candidates are selected, Ansys Maxwell and JMAG Designer are used for detailed loss and performance evaluations in this step.

In the powertrain system, not only the machine itself needs to be evaluated, but also the machine and its system i.e. converter and battery. Hence, the whole procedure is assumed to end up with placing the machine into a system simulation set-up. However, the direct coupling between the finite element model and the control circuit leads to a very slow simulation speed. Therefore, reduced order modelling is necessary to avoid the time-consuming full FEM simulation, especially for the PWM excitation. In this stage, Ansys Twin Builder and JMAG-RT together with Simulink are utilized to generate the ROMs.

Of great importance is to acquire as correct data as possible in each procedure step. Thus, the results of the software are compared using one of the designs, in order to identify if any discrepancies exist.

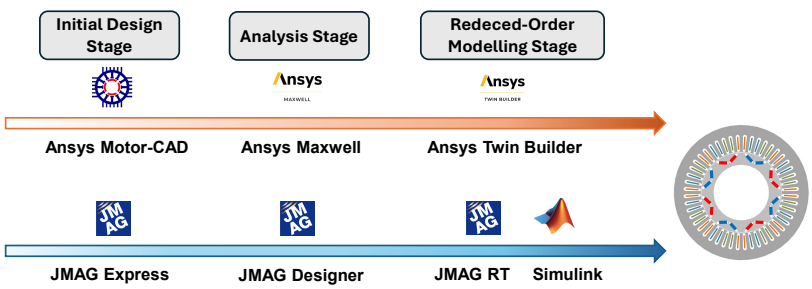

Figure 4.1: Proposed design and analysis process

4.2.2 Comparison Rules

In the proposed design and analysis process, Ansys Maxwell, Motor-CAD, and JMAG Designer are utilized to analyze the machine characteristics and electromagnetic performance. To fairly compare the simulation results of two parallel tracks, some basic comparison rules should be mentioned at the beginning,

- The system configuration should be the same.
- Both the geometry and design parameters of the PMSM should be set identically.
- The identical material properties of magnets, stator and rotor iron, as well as the configurations of windings are defined.
- The same time resolution shall be used.
- The mesh qualities are basically consistent.
- The same current and angle intervals are used when generating ROMs.
- The same operating points shall be simulated.

4.3 Initial Design Stage

The main purpose of the initial design stage is to determine the dimensions and the slot/pole combination. Considering the dimension and power requirement of the powertrain system, the design parameters of the reference PMSM is listed in Section 3.2. After the design parameters are determined, machine characteristics such as efficiency maps need to be evaluated. The efficiency maps from Ansys Motor-CAD and JMAG Express are compared in Fig. 4.2. However, it can be observed that two software present different efficiency results and JMAG Express gives the higher efficiency for all the regions. A hypothesis is made that the discrepancy is caused by the different correction methods for PWM losses or temperature. Therefore, detailed evaluations need to be carried out in the following stages.

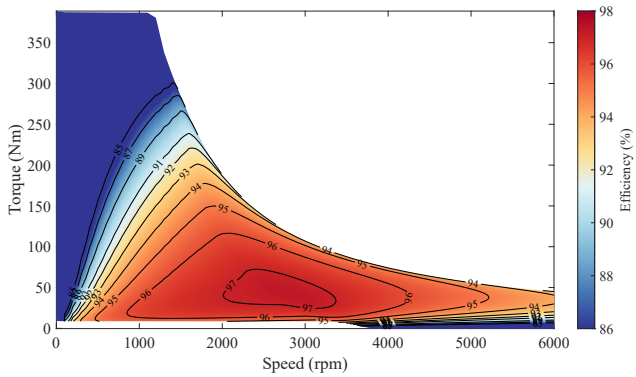

(a) Ansys Motor-CAD

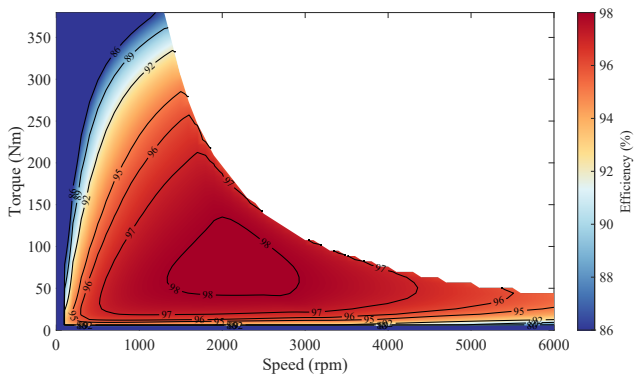

(b) JMAG Express

Figure 4.2: Efficiency map comparison between Ansys Motor-CAD and JMAG Express

4.4 Analysis Stage

The analysis stage focuses on electromagnetic analysis including the no-load and load conditions. For load condition, two representative operating points are selected, denoted OP1 and OP2 which are illustrated in Fig. 4.3.

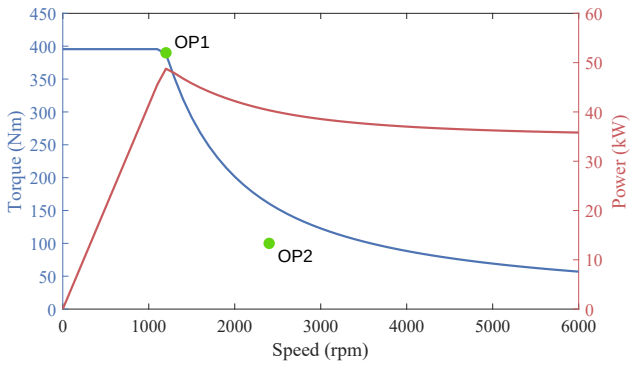

Figure 4.3: The torque/speed curve with selected operating points

Ansys Maxwell and JMAG Designer are used as the evaluation tools at this stage. However, for the purpose of cross-check, the results of Motor-CAD are also included in this section. The transient solver is used for FEM simulations during this stage. To reach the steady state of core loss, the simulation cycle is two electric periods, but only the results for one electric period are presented in this section due to the symmetry.

No-Load Condition

In no-load condition, flux linkage, back-EMF radial flux density and radial force are mainly compared. The simulated back-EMF waveform is presented in Fig. 4.4a. It can be seen in the figure that the waveforms simulated by these software are similar. However, Motor-CAD gives more oscillations, which possibly caused by the mesh disturbance using the imported geometry.

The flux linkage of Phase A is also given in Fig. 4.4b. It can be seen in the figure that the waveforms simulated by these software are similar and the maximum values are 0.1427 Wb using Maxwell, 0.143 Wb using Motor-CAD and 0.1427 Wb using JMAG respectively.

To analyze the radial force, the radial flux density needs to be compared first. The radial flux density is given in Fig. 4.4c. It can be seen that Motor-CAD gives more oscillations in amplitude. Accordingly, the radial force density behaves in the same way as the radial flux density as is shown in Fig. 4.4d. Since the dimension of the reference PMSM is the same in these software, the waveforms of radial force can be easily determined from the aforementioned analysis.

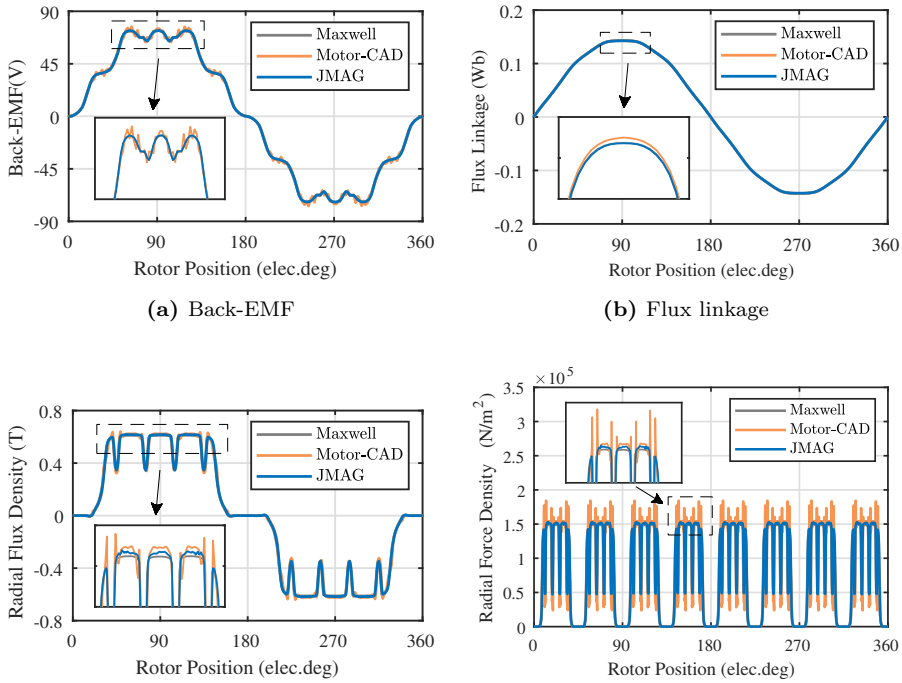

(a) Back-EMF **(b)** Flux linkage

(c) Radial flux density **(d)** Radial force density

Figure 4.4: Electromagnetic comparisons of back-EMF, flux linkage, radial flux density and force at no-load condition

Load Condition

For OP1, the speed is 1200 rpm, and fed by the rated current with 45 degrees phase advance angle. The flux density plot is shown in Fig. 5.6a. The left

half part is from Maxwell and the right one is from JMAG, and the maximum flux density is 2.772 T and 2.789 T respectively. The torque waveforms are illustrated in Fig. 4.5b. The average torque values are 374.7 Nm using Maxwell, 376 Nm using Motor-CAD and 377.4 Nm using JMAG respectively. Accordingly the maximum discrepancy is less than 0.75%. The torque ripple values are 11.9% using Maxwell, 12% using Motor-CAD, 11.7% using JMAG respectively.

The simulated flux linkage waveforms are shown in Fig. 4.5c. It can be seen in the figure that the waveforms simulated by Maxwell and JMAG are similar and the maximum values are 0.3803 Wb and 0.38 Wb respectively. However, in Motor-CAD, the maximum value of flux linkage is 0.4058 Wb and the maximum discrepancy increased to 6.5%.

Compared to the no-load condition, the speed is maintained the same, but the input current increased to 500A with 45 degrees phase advance angle at OP1. Hence, the input current and phase advance angle become the potential factor that affect the maximum discrepancy of flux linkage in Motor-CAD. In order to investigate the relation between the discrepancy and input current and phase advance angle, a contour plot in the polar coordinate system has been created and shown in Fig. 4.6. In this plot, the speed is maintained at 1200 rpm, and the input current changes from 100 to 500 A with the phase advance angles varying from 0 to 90 degrees. It can be seen that the maximum discrepancy of flux linkage is highly related to the input current with different phase advance angles. With an increasing input current and phase advance angle, the maximum discrepancy of flux linkage is increasing, and vice versa.

The comparison of core loss is presented in Fig. 4.7a. Motor-CAD gives higher losses both in the stator and rotor compared to the other two. And it should be mentioned that core losses in Motor-CAD can be calculated using either the Bertotti (Classical or Maxwell) or Steinmetz models which give different values as shown in Fig. 4.7b. The difference of curve fitting techniques and core loss models in these software could predict the different coefficients and core loss values.

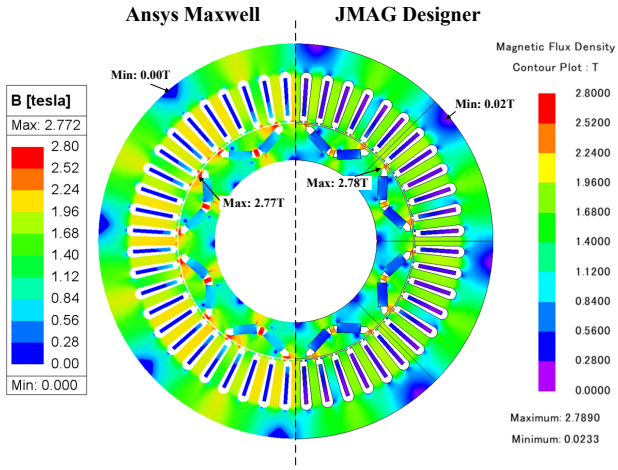

(a) Flux density

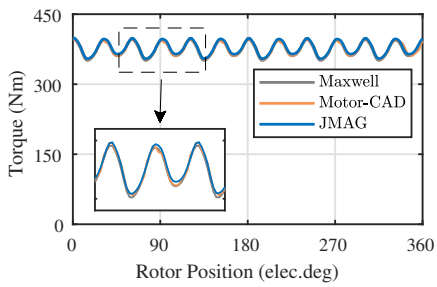

(b) Torque

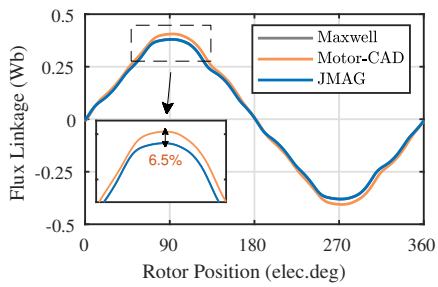

(c) Flux linkage

Figure 4.5: Electromagnetic comparison of flux density, torque and flux linkage at OP1

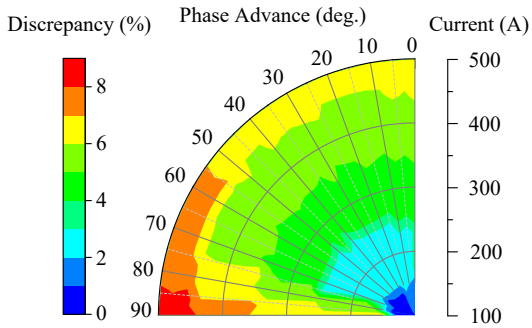

Figure 4.6: Relation between maximum discrepancy and input current with different phase advance angles

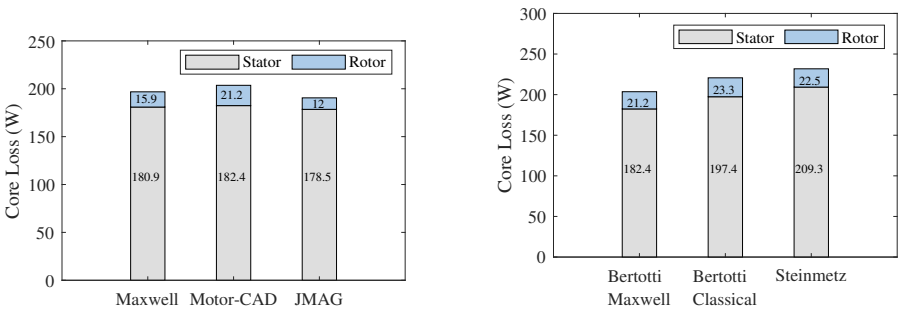

(a) Core loss

(b) Different core loss models in Motor-CAD

Figure 4.7: Core loss comparison with different loss models at OP1

For OP2, the speed is 2400 rpm, and the input current is 100 A with 40 degrees phase advance angle. The torque waveforms are illustrated in Fig. 4.8a. The average torque values are 124.6 Nm using Maxwell, 124.2 Nm using Motor-CAD and 124.5 Nm using JMAG respectively, so the maximum discrepancy is less than 0.35%. The torque ripple values are 24.7% using Maxwell, 27.3% using Motor-CAD, 24.6% using JMAG respectively.

The simulated flux linkage waveforms are shown in Fig. 4.8b It can be seen in the figure that the waveforms simulated by these software are similar and the maximum values are 0.2804 Wb in Maxwell, 0.2813 Wb in Motor-CAD and 0.2793 Wb in JMAG respectively. The maximum discrepancy of flux linkage at OP2 decreases to 0.7% compared to the discrepancy at OP1 Fig. 4.5c. Also, the results correspond with the relation illustrated in Fig. 4.6. That means that the maximum discrepancy of flux linkage in Motor-CAD is more sensitive to the input current with different phase advance angles than the speed.

The comparison of core loss is presented in Fig. 4.8c. JMAG gives lower losses both in the stator and rotor than the others, while Maxwell and Motor-CAD have similar results.

Solving Time

Table 4.1 compares the solving time of three commercial FEM software on the same simulation problem. JMAG Designer 23.1 is the fastest at 39 s, followed by Ansys Motor-CAD 2024.1.1 at 98 s (roughly 2.5× slower), while Ansys Maxwell 2024 R1 takes 457 s, about 12× slower than JMAG.

Table 4.1: Solving Time

Software	Sloving time
Ansys Maxwell 2024 R1	457 s
Ansys Motor-CAD 2024.1.1	98 s
JMAG Designer 23.1	39 s

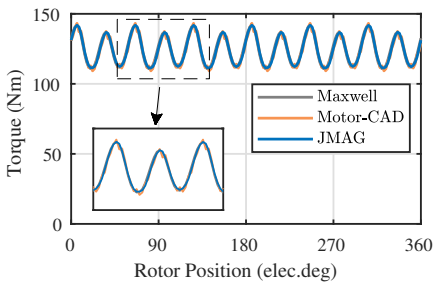

(a) Torque

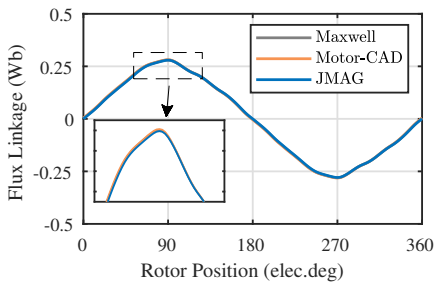

(b) Flux linkage

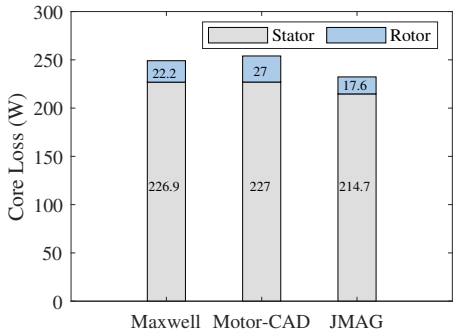

(c) Core loss

Figure 4.8: Electromagnetic comparisons of torque, flux linkage and core loss at OP2

4.5 System-Level Stage

At the system-level stage, the ROMs are utilized for further analysis by coupling PWM excitation or battery packs. To generate the ROMs, the current interval is set to 50A, and the rotor angle interval is set to 15 electric degrees. To verify the accuracy between FEM and ROM simulation results, the speed is set to 1200 rpm, and the input current is 70 A with 0 degree phase advance. The results are compared in Fig. 4.9. It shows that JMAG-RT has better agreement with FEM results, while Ansys Twin Builder has a 2.6 Nm lower value for torque ripple.

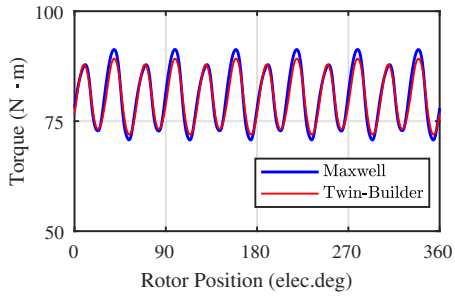

(a) Ansys Twin Builder

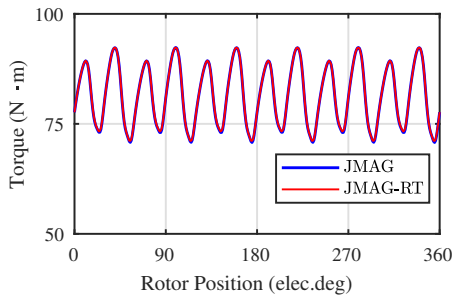

(b) JMAG-RT

Figure 4.9: Simulation results of FEM and ROM with Ansys Maxwell and JMAG

CHAPTER 5

Circuit-Based Spatial Harmonics Model

5.1 Overview

This chapter proposes a computationally efficient method to build a nonlinear PMSM model in polar coordinates, which includes steps of circuit model implementation, flux maps generation and inversion of flux maps.

5.2 Circuit-Based PMSM Models

5.2.1 Lumped-Parameter Model

According to different machines parameters, a lumped-parameter model can be further divided into inductance-based model and flux-based model. In this chapter, flux-based model is the main focus, which can be expressed as

$$\boldsymbol{u_s} = R_s \boldsymbol{i_s} + \frac{d\boldsymbol{\psi_s}}{dt} + \omega_e \boldsymbol{J} \boldsymbol{\psi_s} \tag{5.1}$$

$$T_e = \frac{3n_p}{2} \mathbf{Im}\{\boldsymbol{i_s} \boldsymbol{\psi_s^*}\} \tag{5.2}$$

where R_s is the stator resistance, ω_e is the electrical rotor speed, T_e is the electromagnetic torque, the stator voltage is $\boldsymbol{u_s} = \begin{bmatrix} u_d & u_q \end{bmatrix}^T$, the stator current is $\boldsymbol{i_s} = \begin{bmatrix} i_d & i_q \end{bmatrix}^T$, the stator flux linkage is $\boldsymbol{\psi_s} = \begin{bmatrix} \psi_d & \psi_q \end{bmatrix}^T$, and the orthogonal rotational matrix is $\boldsymbol{J} = \begin{bmatrix} 0 & -1 \\ 1 & 0 \end{bmatrix}$.

It can be seen that the lumped-parameter model can be easily implemented due to the fixed parameters and linear characteristics. However, it will only be accurate under the condition where the PMSM is not saturated.

5.2.2 Saturation Model

Due to the fixed parameters, the lumped-parameter model cannot describe the saturation phenomenon in a PMSM. To overcome this issue, a nonlinear model with dynamic flux data has been used. In this model, the flux data are based on the d- and q-axis current which can represent the saturation phenomenon in a PMSM, giving a proposed equation setup as

$$\boldsymbol{u_s} = R_s \boldsymbol{i_s} + \frac{d\boldsymbol{\psi_s}(i_d, i_q)}{dt} + \omega_e \boldsymbol{J} \boldsymbol{\psi_s}(i_d, i_q) \tag{5.3}$$

$$T_e = \frac{3n_p}{2} \mathbf{Im}\{\boldsymbol{i_s} \boldsymbol{\psi_s^*}(i_d, i_q)\} \tag{5.4}$$

In this model, the flux data are obtained from the average of flux linkage ignoring the rotor position. Hence, the spatial harmonics effects cannot be reflected in this saturation model.

5.2.3 Spatial Harmonics Model

To further improve the fidelity of the PMSM model, the spatial harmonics need to be considered. The spatial harmonics components can be reflected by the rotor position with respect to the stator slots and teeth. Hence, compared to the saturation model, rotor position is added to this model as the third dimension to reflect the spatial harmonics effect in a PMSM, which can be expressed as

$$\boldsymbol{u_s} = R_s \boldsymbol{i_s} + \frac{d\boldsymbol{\psi_s}(i_d, i_q, \vartheta)}{dt} + \omega_e \boldsymbol{J} \boldsymbol{\psi_s}(i_d, i_q, \vartheta) \tag{5.5}$$

$$T_e = \frac{3n_p}{2}\mathbf{Im}\{\boldsymbol{i_s}\boldsymbol{\psi_s^*}(i_d, i_q, \vartheta)\} \tag{5.6}$$

where ϑ is the rotor position.

At this point, the nonlinear effects of cross-coupling, saturation, and spatial harmonics have been integrated, and ultimately increase the fidelity of the model.

5.3 Proposed Method

5.3.1 Circuit Model

Based on the PMSM voltage equation, the circuit-based model can be expressed as

$$\boldsymbol{\psi_s}(i_d, i_q, \vartheta) = \int (\boldsymbol{u_s} - R_s\boldsymbol{i_s} - \omega_e\boldsymbol{J}\boldsymbol{\psi_s}(i_d, i_q, \vartheta))dt \tag{5.7}$$

According to the spatial harmonics model (5.5), the block diagram of the circuit model can be illustrated in Fig.5.1.

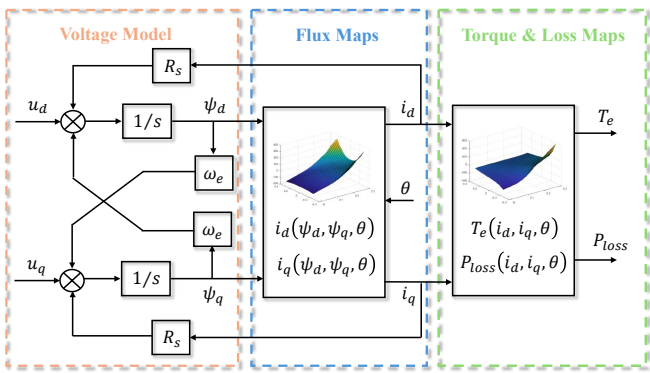

Figure 5.1: Circuit Model

5.3.2 Flux Maps in Cartesian Coordinates

Generally, flux maps are utilized to represent the electromagnetic model of PMSM, and the d- and q-axis flux linkages are expressed as a function of d- and q-axis current in Cartesian Coordinates, shown in Fig. 5.2.

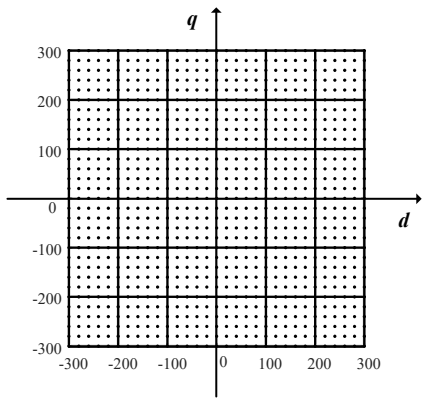

Figure 5.2: Grid points of flux Maps in Cartesian Coordinates

The flux maps including the d- and q-axis flux linkages and torque $\psi_d(i_d, i_q, \vartheta)$, $\psi_q(i_d, i_q, \vartheta)$, $T_e(i_d, i_q, \vartheta)$ are extracted from FEM simulation by varying the given parameters of d- and q-axis current i_d, i_q and rotor position ϑ, can be expressed as

$$\begin{cases} \psi_d = f(i_d, i_q, \vartheta) \\ \psi_q = g(i_d, i_q, \vartheta) \end{cases} \tag{5.8}$$

The range of i_d, i_q is [-300,300] A, with steps of 5A per division. The range of rotor position ϑ is [0, 360] electrical degrees, with steps of 1 degree per division.

5.3.3 Flux Maps in Polar Coordinates

The flux maps method in Cartesian coordinates can generate symmetric matrices with a monotonic function of flux linkage, which is beneficial for matrix inversion and interpolation.

However, according to the operating region of PMSMs, at least 21.4% of the results points when using the Cartesian method are not necessary for modelling, as shown in Fig. 5.3. Therefore, a new modelling method in polar coordinates to avoid computational burden is proposed this paper, which can be illustrated in Fig.5.4.

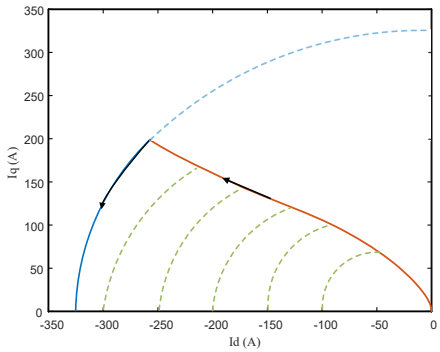

Figure 5.3: PMSM Operating Region

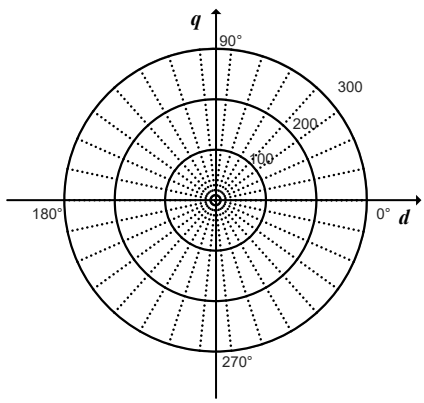

Figure 5.4: Grid points of flux Maps in Polar Coordinates

In polar coordinates, the flux linkage, flux angle and torque $\psi_s(i_s, \gamma, \vartheta)$, $\varphi(i_s, \gamma, \vartheta)$, $T_e(i_s, \gamma, \vartheta)$ are extracted from FEM simulation by varying parameters of stator current i_s, current angle γ and rotor position ϑ. The flux

linkage and flux angle extracted from FEM simulation with given stator current, current angle and rotor position can be expressed as

$$\begin{cases} \psi_s = f(i_s, \gamma, \vartheta) \\ \varphi = g(i_s, \gamma, \vartheta) \end{cases} \tag{5.9}$$

The range of i_s is [0, 300] A with steps of 5A. The range of current angle γ is [0, 360] electrical degrees, with steps of 2 degrees per division. The range of rotor position ϑ is [0, 360] electrical degrees, with steps of 1 degree per division.

5.3.4 Inverse Flux Maps

According to the PMSM voltage equation and the previous circuit model, the flux maps need to be inverted, with the outputs being the d- and q-axis current. In previous steps, the parameters for generating flux maps are stator current and current angle. And accordingly, the parameters of inverting flux maps could preferably be flux linkage and flux angle. However, from mathematical perspectives, the magnitude of the flux linkage does not vary monotonically with the current angle, which means that a single flux magnitude may correspond to multiple current angles. This can lead to failure during matrix inversion or interpolation.

Therefore, a transformation is added to the process of inversion flux maps. After the transformation, the minimum and maximum values of ψ_d and ψ_q are determined based on previous flux maps and the intervals are subdivided into n divisions ($n = 60$). Then, the correlation matrix of current and flux linkage can be inverted and interpolated utilizing curve fitting tools, which can be written as,

$$\begin{cases} i_d = f^{-1}(\psi_d, \psi_q, \theta) \\ i_q = g^{-1}(\psi_d, \psi_q, \theta) \end{cases} \tag{5.10}$$

As mentioned above, the flux maps in (5.8) has three dimensions, and the third dimension is the rotor position which is stored as pages in MATLAB. Hence, the idea of the inverse flux maps is that the flux maps can be decomposed through the pages and inverted page by page. After the inversion process, the new flux map can be composed again to a new map according to the pages. Finally, these flux maps will contain spatial harmonics components

by applying the map inversion to each rotor position. This inversion process can be illustrated in Fig. 5.5. Only four values of rotor position are shown for clarity.

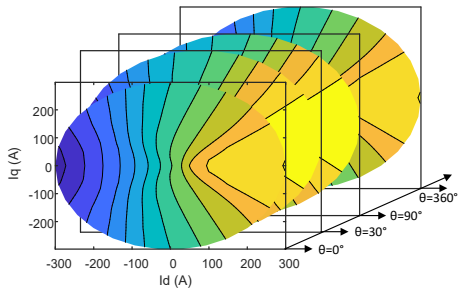

Figure 5.5: Inverse Flux Maps Method

Finally, the electromagnetic toruqe and core loss can be obtained based on the output current which is shown in Fig.5.1, and can be expressed as

$$\begin{cases} T_e = T(i_d, i_q, \theta) \\ P_{loss} = P(i_d, i_q, \theta) \end{cases} \tag{5.11}$$

5.4 Results

5.4.1 Inverse Flux Maps

The d- and q-axis flux linkage table generated from FEM simulation is illustrated in Fig. 5.6. It can be seen that the flux maps captured the nonlinear characteristics of PMSM, and the proposed method covered less unnecessary region compared to the Cartesian method, which means the proposed method is more time-efficient. Based on the flux maps generated from FEM simulation, the inverse maps can be obtained which are shown in Fig. 5.7a and Fig. 5.7b, respectively. It can be seen that the flux maps are inverted successfully and the inverse maps can reflect the saturation and spatial harmonics characteristics of the PMSM.

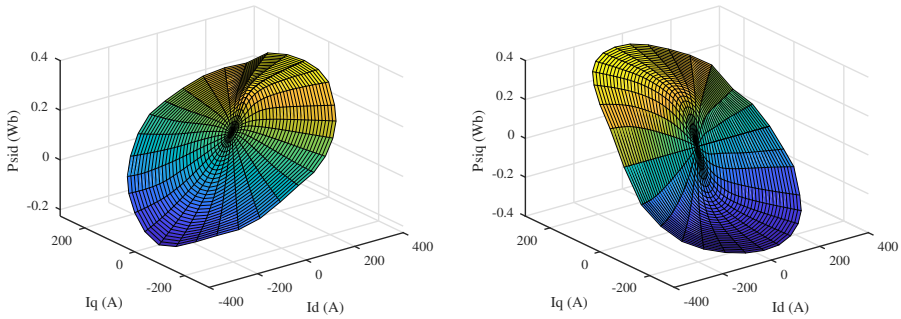

(a) d-axis Flux Linkage **(b)** q-axis Flux Linkage

Figure 5.6: Flux Maps at $\theta = 0$

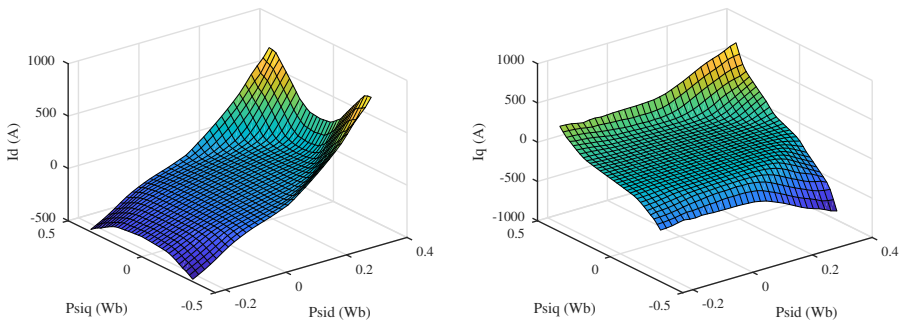

(a) d-axis Current **(b)** q-axis Current

Figure 5.7: Inverse Flux Maps at $\theta = 0$

5.4.2 Model Verification

After having imported the inverse maps, the circuit model is implemented in MATLAB/Simulink to verify it. The input sinusoidal voltage is set as 60V, 80Hz, and the rotation speed is 1200rpm. The flux linkage of Phase A is given in Fig. 5.8a. It can be seen that the waveforms of FEM and the proposed model are identical, which means that the original d-q flux data extracted from FEM has been inversed successfully.

The simulated Phase A current waveform is presented in Fig. 5.8b. It can be seen in the figure that the waveforms simulated by FEM and the proposed model have a good agreement. The torque is also given in Fig. 5.8c. For core loss, the FEM result is a constant value and the result of proposed model has some ripple which is illustrated in Fig. 5.8d.

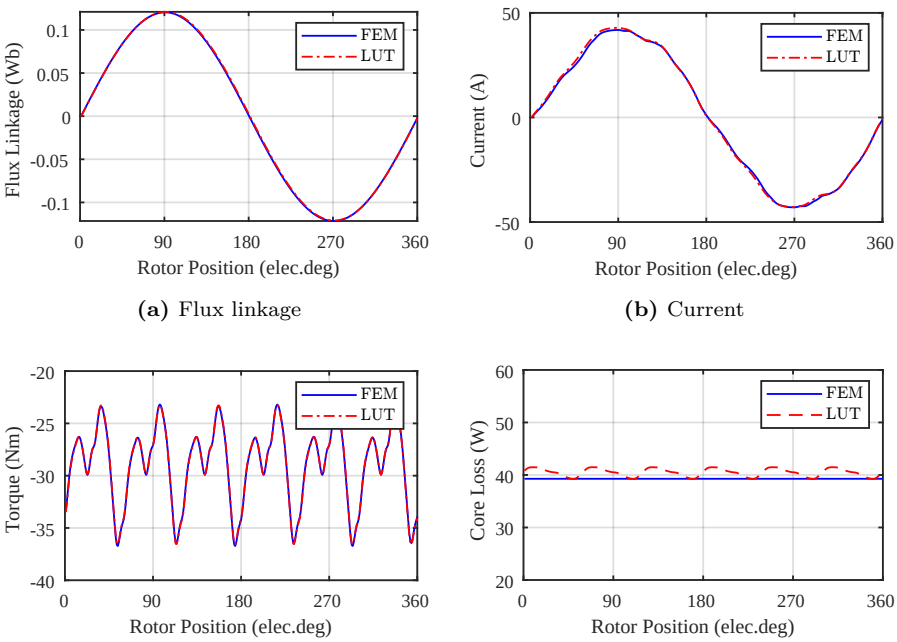

(a) Flux linkage

(b) Current

(c) Torque

(d) Core loss

Figure 5.8: Results Comparisons between the FEM and the proposed Model

5.4.3 Dynamic Performance

After the comparison with FEM, the dynamic analysis is implemented. To verify the dynamic performance of this model, the current controllers are added to the circuit model. The input reference current and output current is shown in Fig. 5.9a. The d- and q-axis flux linkage are illustrated in Fig. 5.9b. It can be seen that the dynamic response of the proposed model can follow the reference current command which shows the accuracy and stability of this model.

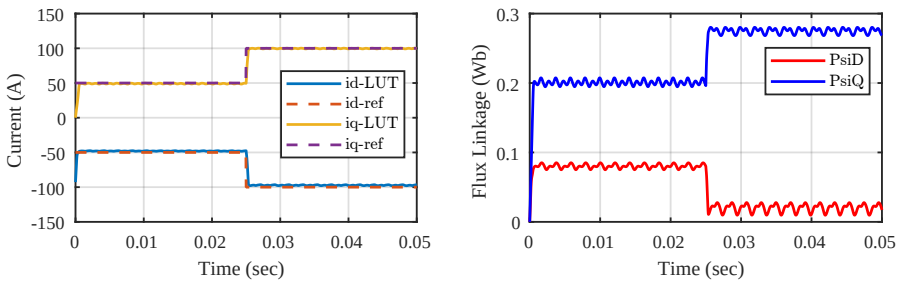

(a) D-axis and q axis current

(b) D-axis and q axis flux linkage

Figure 5.9: Dynamic Performance

5.4.4 FEM Solving Time

From the previous section, it is known that there are 3721 and 2806 cases for the Cartesian method and the proposed method, respectively. Ideally, the FEM solving time should be identical for each case which means that the proposed method can reduce the FEM solving time by 21.4%.

However, in JMAG Designer, the measured FEM solving time is increasing nonlinearly with the number of cases, which is shown in Fig. 5.10a. Accordingly, the cumulative solving time is also increasing nonlinearly which is shown in Fig. 5.10b. The possible reason for explaining this phenomenon is that frequent read/write activities and their patterns trigger the security scan of Microsoft Defender Antivirus in Windows 10, which slow down the FEM simulation.

For generating flux maps, this nonlinear increase means that the last 21.4% of cases accounts for nearly 45% of the total solving time. In other words, the

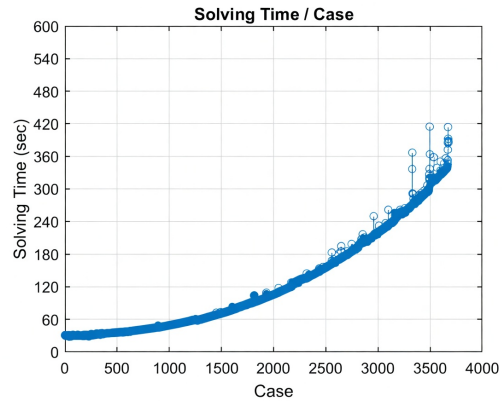

(a) Solving time per case

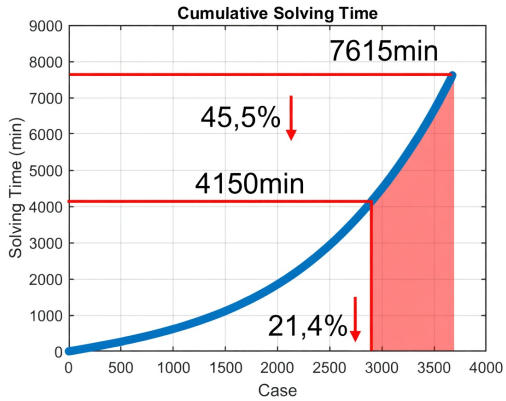

(b) Cumulative solving time

Figure 5.10: Measured FEM solving time in JMAG

proposed method not only reduces the 21.4% of unnecessary points in polar coordinates but in fact save 45% of the total FEM solving time.

Finally, the solving time comparison between the Cartesian method and the proposed method is shown in Table 5.1, respectively. It shows that the proposed method can significantly reduce the solving time while maintaining the accuracy of the model.

Table 5.1: FEM Solving Time

Method	Number of FEM Cases	FEM Solving Time
Cartesian Coordinates	3721	7615
Polar Coordinates	2806	4150

CHAPTER 6

Design-Oriented Torque Ripple Mitigation Methods

6.1 Overview

This chapter focuses on design-oriented torque ripple mitigation methods. The reference PMSM used in this chapter is shown in Case setup 2. The no-load characteristic including the cogging torque, flux linkage, back-EMF, and the load characteristic including torque ripple are analyzed in the beginning. Based on this, design-oriented methods including skewing, notching, and geometry optimization are investigated and compared.

6.2 Torque Ripple Analysis

6.2.1 No-Load Analysis

The cogging torque and harmonics in back-EMF which induces torque ripple are analyzed in this section.

Cogging Torque

First, to investigate the cogging torque, the speed is set as 1 rpm without current excitation in the simulation, isolating the magnet–slot reluctance interaction. The cogging toque in shown in Fig. 6.1.

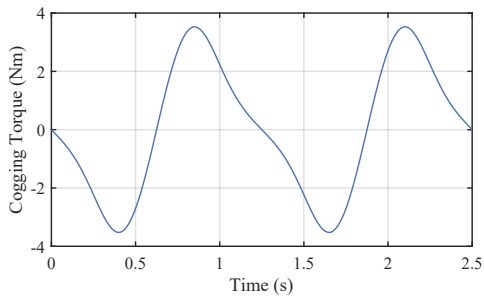

Figure 6.1: Cogging torque at 1 rpm

The number of periods of the cogging toque which is utilized in the skewing method, can be calculated as

$$N_{cogging} = \frac{2N_pN_s}{LCM(N_s, 2N_p)} \tag{6.1}$$

Flux Linkage

Then, the flux linkage at 2000 rpm and its fast Fourier transform (FFT) analysis are investigated, which are shown in Fig. 6.2. The waveform reveal the periodic distortion caused by, while the FFT identifies the dominant low-order harmonic components, primarily the 5th, 7th, 11th, and 13th orders, along with their magnitudes and phase with respect to the fundamental. These spectral characteristics provide the information for the harmonic injection method.

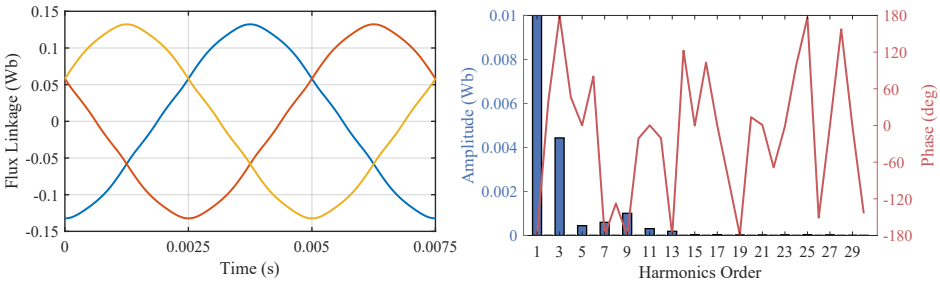

(a) Flux linkage waveform **(b)** FFT analysis with amplitude and phase

Figure 6.2: No load flux linkage waveform and FFT analysis at 2000 rpm

Back-EMF

Similarly, the back-EMF at 2000 rpm and its FFT analysis are investigated, which are shown in Fig. 6.3.

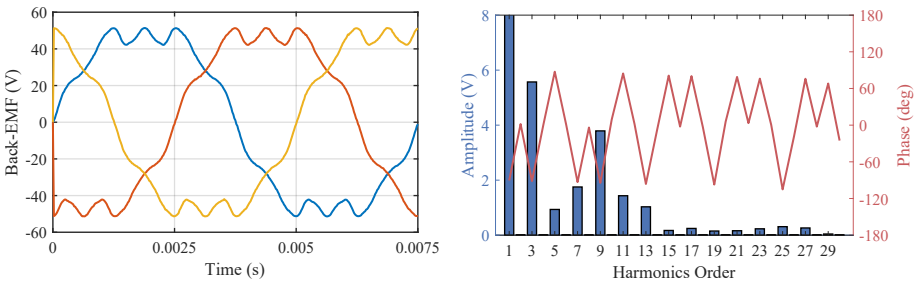

(a) Back-EMF waveform **(b)** FFT analysis with amplitude and phase

Figure 6.3: No load back-EMF waveform and FFT analysis at 2000 rpm

6.2.2 Load Analysis

To investigate the torque ripple, a specific operating point is selected for analysis and illustrated in Fig. 6.4. At this point, the PMSM is operating at 2000 rpm, fed by 380 A RMS sinusoidal current with 47.1 deg.

The torque ripple and FFT analysis are shown in Fig. 6.5. It can be seen that the 12th torque ripple is dominant in this reference PMSM.

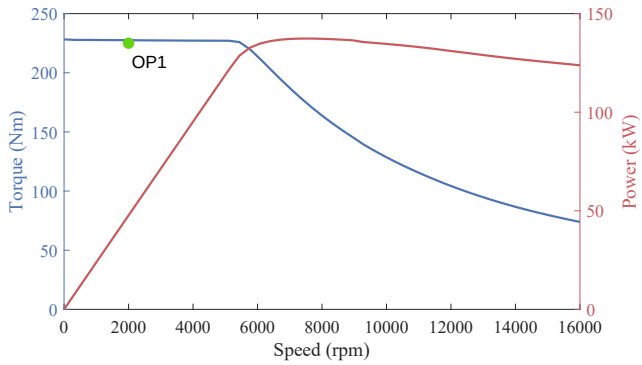

Figure 6.4: The torque/speed curve with selected operating points

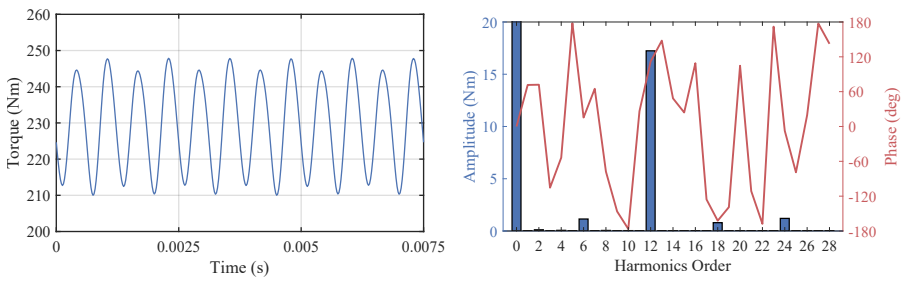

(a) Torque ripple

(b) FFT analysis with amplitude and phase

Figure 6.5: Torque ripple and FFT analysis at operating point

6.3 Design-Oriented Methods

In this section, three design-oriented mitigation methods from rotor side will be discussed including skewing, auxiliary notch and geometry optimization.

6.3.1 Skewing

From the previous analysis, the skewing can be applied both to the stator and the rotor. Besides, there are several types of skewing patterns. Considering manufacturability of hairpin windings and permanent magnets in the automotive industry, this section will focus on the rotor skewing.

Step Skewing

The skew angle and the reference cross section in step skewing are illustrated in Fig. 6.6. It can be seen that there are different reference cross sections with odd or even number of slices.

Fig. 6.7 compares the torque ripple with different number of slices and skew angles using step skew. The range of number of slices is from 2 to 5, and skew angle is from 0 to 15 degrees.

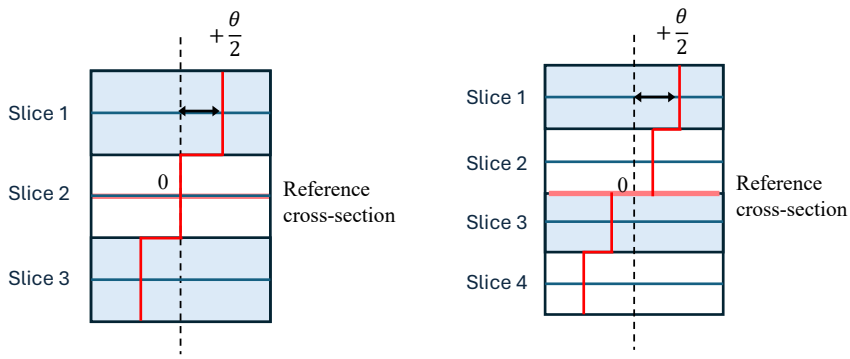

(a) Odd number of slices **(b)** Even number of slices

Figure 6.6: Skew angle definition in step skewing

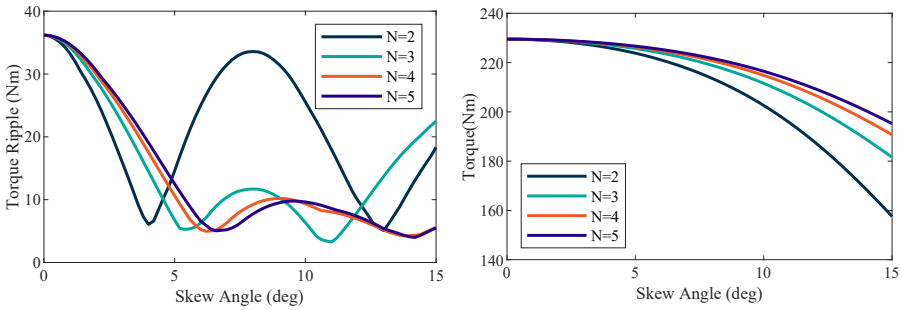

(a) Torque ripple **(b)** Average torque

Figure 6.7: Step skewing

V-Type Skewing

Similarly, the skew angle and the reference cross section in V-type skewing are illustrated in Fig. 6.8. Fig. 6.9 shows the torque ripple with different skew angle and slices using V-type skew. The range of number of slices is from 3 to 6, and skew angle is from 0 to 15 degrees.

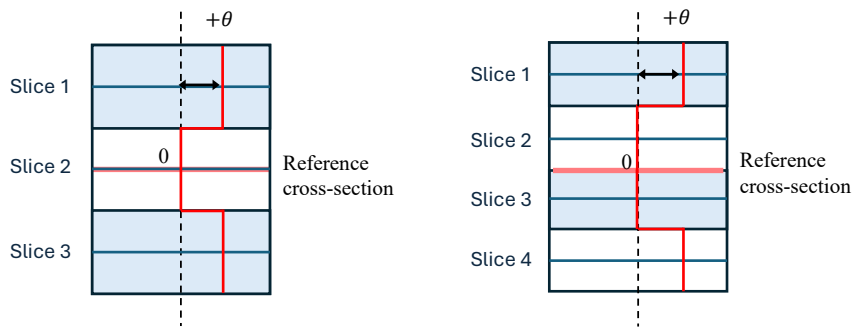

(a) Odd number of slices **(b)** Even number of slices

Figure 6.8: Skew angle definition in V-type skewing

However, skewing not only increase the manufacturing cost but also generate axial electromagnetic force, which raise the risk of bearing loss, noise, demagnetization and reduced lifespan [22].

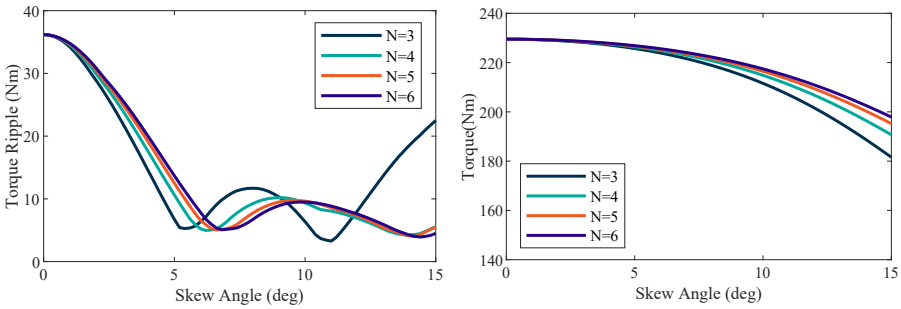

(a) Torque ripple **(b)** Average torque

Figure 6.9: V-type skewing

6.3.2 Auxiliary Notch

Auxiliary notches are another rotor shape modification method to mitigate torque ripple. In this paper, elliptical-shape notches are selected and investigated among the different shape variants shown in Fig. 6.10. In order to find the optimal parameters, a parametric sweep is conducted with the ranges of the parameters listed in Table 6.1.

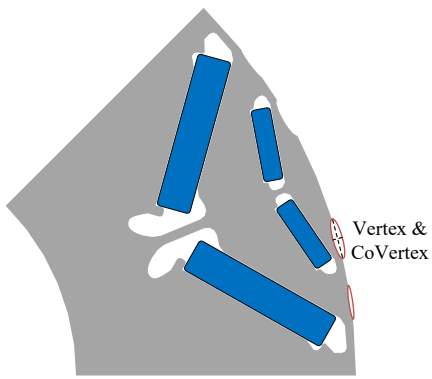

Figure 6.10: Rotor topology with double notches

Fig. 6.11 shows the results of all cases, and the Pareto front of optimal notch

Table 6.1: Notch Design Parameters

Parameter	Value
Inner_Notch_Vertex	0.1-3.1 mm
Inner_Notch_CoVertex	0.1-0.7 mm
Outer_Notch_Vertex	0.1-3.1 mm
Outer_Notch_CoVertex	0.1-0.7 mm

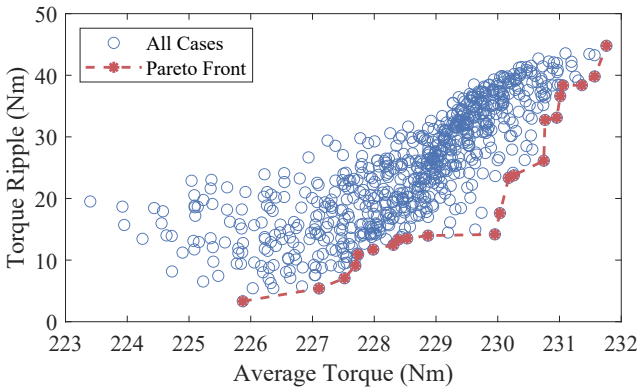

Figure 6.11: Pareto front and feasible solutions

parameters. It can be seen that, compared to skewing, auxiliary notches lose average torque less while mitigating the ripple. However, only few cases can reach same performance compared to skewing, and it will be time-consuming to find the optimal point.

6.3.3 Geometry Optimization

Geometry optimization is a comprehensive option to further minimize the torque ripple. The design parameters and their range which could to be optimized are listed in Table 6.2 and shown in Fig. 6.12. The sensitivity analysis of these parameters is carried out first. Fig. 6.13 shows the correlation plot of design parameters and sensitivity values.

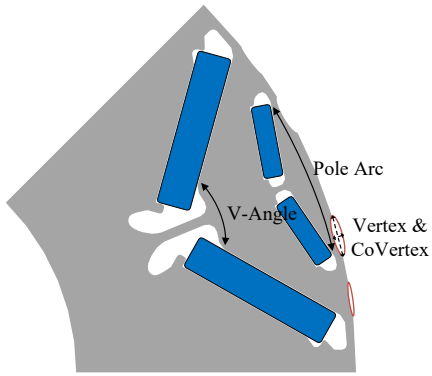

Figure 6.12: Rotor topology with optimization parameters

Table 6.2: Optimization Parameters

Parameter	Value
M1_Pole_Arc	16-20
M1_Pole_V_Angle	110-130
M2_Pole_Arc	8-11
M2_Pole_V_Angle	100-130
Inner_Notch_Vertex	0.1-3.1 mm
Inner_Notch_CoVertex	0.1-0.7 mm
Outer_Notch_Vertex	0.1-3.1 mm
Outer_Notch_CoVertex	0.1-0.7 mm

Based on the sensitivity analysis, the genetic algorithm based multi-objective optimization is utilized to find optimal design of this PMSM. The number of generation and population sizes are 30 and 50, respectively. The parallel coordinate plot shows the optimal case and other cases with their design parameters in Fig. 6.14.

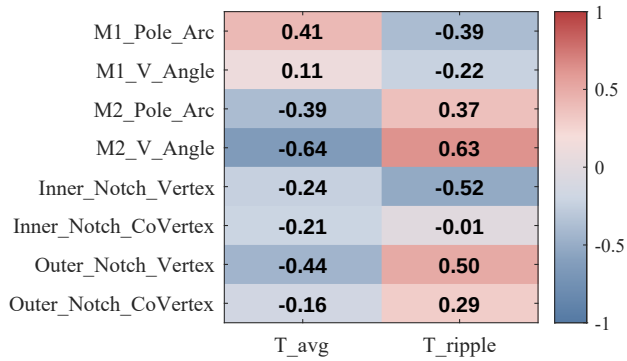

Figure 6.13: Correlation plot of design parameters and sensitivity values

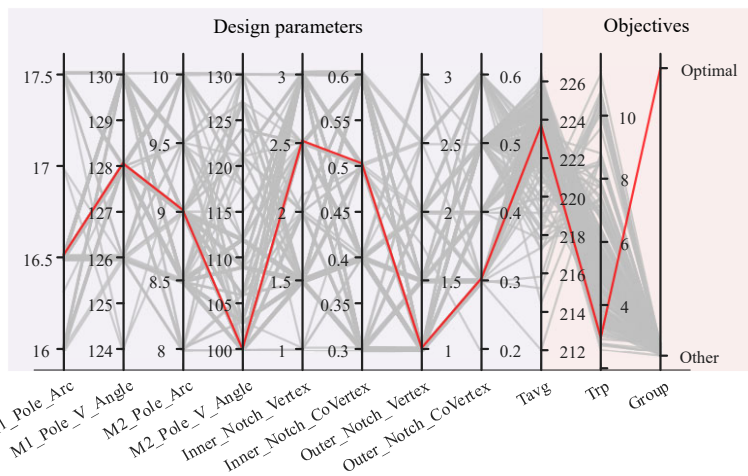

Figure 6.14: Parallel coordinate plot of variables and objectives

6.4 Summary

The summary table of the design-oriented methods is shown in Table 6.3. It can be seen that all methods substantially reduce torque ripple, from 37.8 Nm down to 2.6 – 6 Nm, corresponding to 84.1 – 93.1% reduction, at the cost of a modest average-torque penalty of 1.6–2.8%. Step-skewing and V-skewing achieve comparable ripple reductions (84.1% and 86.2%) with similar average torque losses, indicating that the additional manufacturing complexity of V-skewing yields limited benefit over step-skewing in this case. The auxiliary notch approach delivers a better ripple reduction of 91.2% with the same 1.6% average torque drop compared to step-skewing. The geometry-optimization result achieves the lowest torque ripple at 2.6 Nm (93.1% reduction), but with the largest average torque penalty (2.8%), reflecting the typical torque ripple-average torque trade-off encountered in rotor-shape optimization.

In summary, design-oriented approaches can effectively mitigate torque ripple to some extent without losing too much average torque. However, design modifications will increase the manufacturing cost. Hence, control-oriented approaches need to be investigated.

Table 6.3: Summary Table

Methods	Average Torque	Torque Ripple
Reference	229.5 Nm	37.8 Nm
Step-Skewing	225.9 Nm (1.6% ↓)	6 Nm (84.1% ↓)
V-Skewing	225 Nm (2% ↓)	5.2 Nm (86.2% ↓)
Auxiliary Notch	225.9 Nm (1.6% ↓)	3.3 Nm (91.2% ↓)
Optimization	223 Nm (2.8% ↓)	2.6 Nm (93.1% ↓)

CHAPTER 7

Control-Oriented Torque Ripple Mitigation Methods

7.1 Overview

This chapter focuses on the control-oriented torque ripple mitigation method based on harmonic current injection. The reference PMSM used in this chapter is the same one analyzed in Chapter 6. First, the harmonic current injection method is analyzed and implemented in FEM software. Furthermore, a stochastic gradient descent based method is proposed for decomposing harmonics.

7.2 Harmonic Current Injection

7.2.1 Effectiveness Validation

From the previous analysis in Chapter 6, it can be seen that the torque ripple and back-EMF contain different orders of harmonics. Therefore, to mitigate torque ripple utilizing the HCI method, the sensitivity analysis between torque ripple and injected harmonics needs to be investigated.

From Fig. 6.2 and Fig. 6.5, the $6k$th order harmonic components are domi-

nant in torque ripple which are corresponding to the $(6k \pm 1)$th order current harmonics in the three phase system. Additionally, taking the 6th order harmonic component as an example, the -5th order is classified as the negative sequence component and the +7th order is classified as the positive sequence component in the three phase system. Fig. 7.1 illustrates the relationship between the positive and negative sequence components.

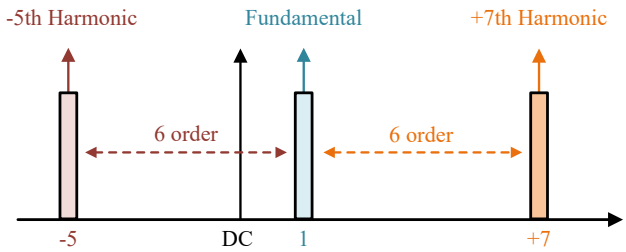

Figure 7.1: Relationship between positive and negative sequence component

The injected positive sequence harmonics can be expressed as

$$\begin{cases} i_a = \lambda_p \cdot I_m e^{j(k\omega_e t + \varphi_p)} \\ i_b = \lambda_p \cdot I_m e^{j(k\omega_e t - 2/3\pi + \varphi_p)} \\ i_c = \lambda_p \cdot I_m e^{j(k\omega_e t + 2/3\pi + \varphi_p)} \end{cases} \tag{7.1}$$

The injected negative sequence harmonics can be expressed as

$$\begin{cases} i_a = \lambda_n \cdot I_m e^{j(k\omega_e t + \varphi_n)} \\ i_b = \lambda_n \cdot I_m e^{j(k\omega_e t + 2/3\pi + \varphi_n)} \\ i_c = \lambda_n \cdot I_m e^{j(k\omega_e t - 2/3\pi + \varphi_n)} \end{cases} \tag{7.2}$$

where k is the harmonic order, φ_p, φ_n are the phase of the injected current, and $\lambda_p, \lambda_n \in (0, 1)$ is an amplitude ratio between the injected current and fundamental current.

Taking the 5th and 7th injection as an example, the relationship of amplitude and phase between the fundamental and injected current is illustrated in Fig. 7.2.

Hence, the sensitivity analysis starts from the three phase system, and inject current individually. Fig. 7.3 illustrates the 6th torque ripple reduction with

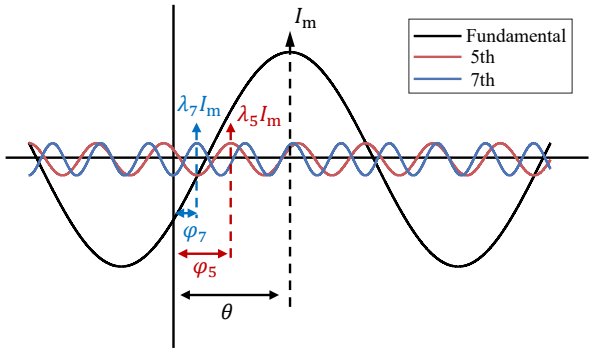

Figure 7.2: Positive and negative sequence component

5th and 7th current injection, respectively. It can be seen that the torque ripple is reduced from 37.8 Nm to 34.9 Nm and 35.4 Nm with the 5th and 7th current injection, respectively.

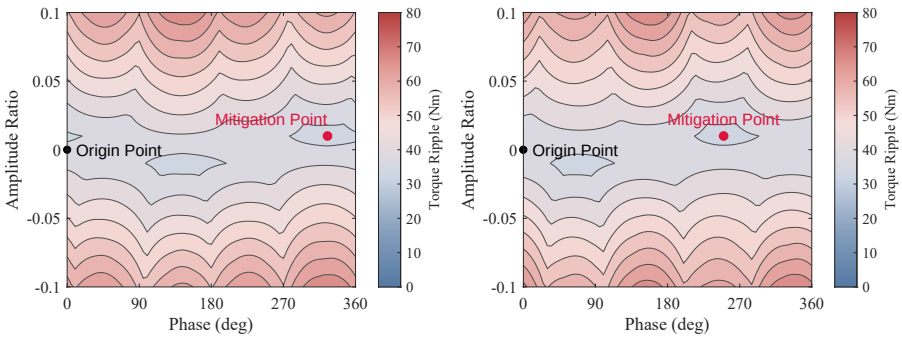

(a) 5th harmonic injection

(b) 7th harmonic injection

Figure 7.3: Torque ripple reduction with individual current injection

Based on the individual injection, the 5th and 7th combined current injection is implemented to mitigate the 6th torque ripple. The amplitude of 5th and 7th harmonic current I_5 and I_7 are selected as $0.01I_m$, the phase are selected as 261 and 303 degrees, and the injected current is shown in Fig. 7.4a. The reduction of torque ripple is relatively small due to the low amplitude of the 5th and 7th harmonics components in this reference PMSM.

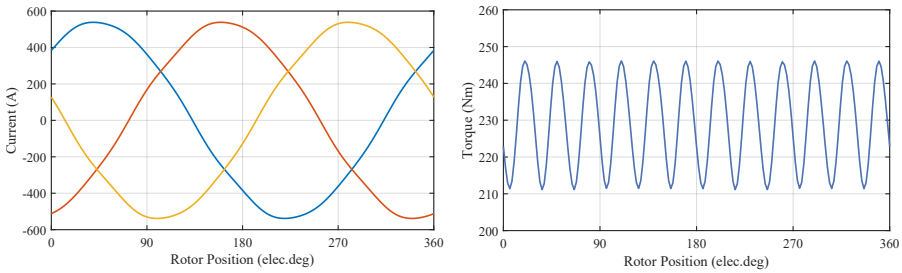

(a) 5th and 7th current injection **(b)** 6th torque ripple reduction

Figure 7.4: Torque ripple reduction with combined current injection

Fig. 7.5 illustrates the 12th torque ripple reduction with the 11th and 13th current injection. It can be seen that the torque ripple is reduced from 37.8 Nm to 5.5 Nm and 6.8Nm with the 11th and 13th current injection, respectively.

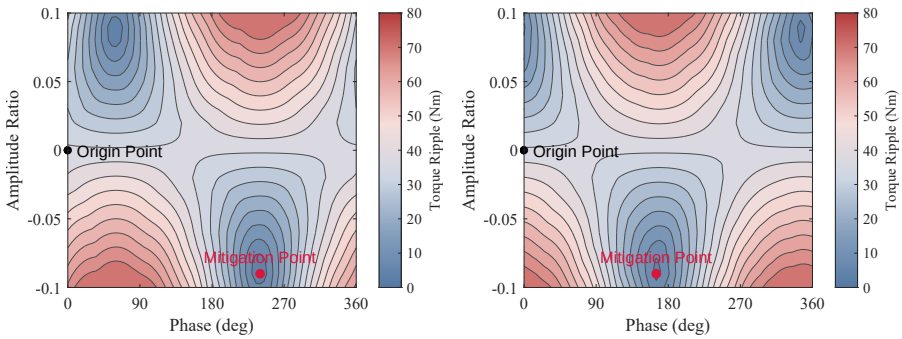

(a) 11th harmonic injection **(b)** 13th harmonic injection

Figure 7.5: Torque ripple reduction with individual current injection

The amplitude of 11th and 13th harmonic current I_{11} and I_{13} are selected as $0.09I_m$, the phase are selected as 1 and 44 degrees, and the injected current is shown in Fig. 7.6a. Since the 12th torque ripple is dominant in the reference PMSM, this combination mitigate torque ripple more effectively.

The results validate the effectiveness of HCI method regarding the torque ripple reduction. Compared to the mitigation performance shown in Table 6.3, the HCI method can reach the same level without hardware modification.

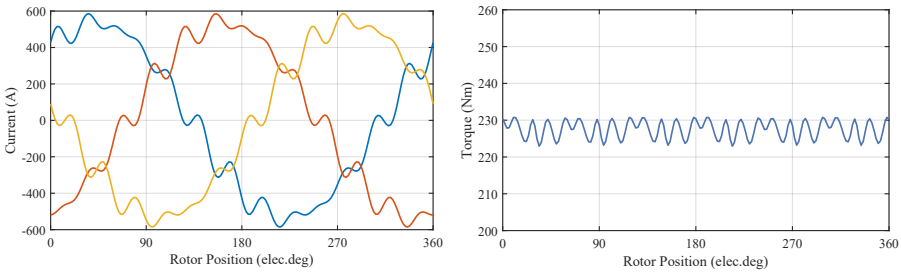

(a) 11th and 13th current injection

(b) 12th torque ripple reduction

Figure 7.6: Torque ripple reduction with combined current injection

7.2.2 Mitigation Performance Comparison

To further compare the mitigation performance, both average torque and torque ripple need to be considered. In order to fairly compare different methods, an objective function is defined as

$$\boldsymbol{J} = \sigma T'_{avg} - (1-\sigma)(T'_{pk2pk})^2 \tag{7.3}$$

where σ is the weighting coefficient, and T'_{avg} and T'_{pk2pk} represent the normalized value of average torque and torque ripple, respectively.

In 7.3, the quadratic term is lenient on small ripples, aggressive on large ripples as it increase much faster. Therefore, maximizing the objective function can provide the knee points for these mitigation methods.

The overall comparison between design-oriented method and harmonics injection method is illustrated in Fig. 7.7. In this figure, the weighting coefficient σ is set as 0.8 to get higher average torque with low torque ripples. Based on the objective function, four knee points from different methods are selected and compared with the original design point.

It can be seen that four knee points give a similar torque ripple level, but the HCI method has a higher average torque that is close to the original case. It can be verified that the HCI method can mitigate torque ripple without losing a large average torque.

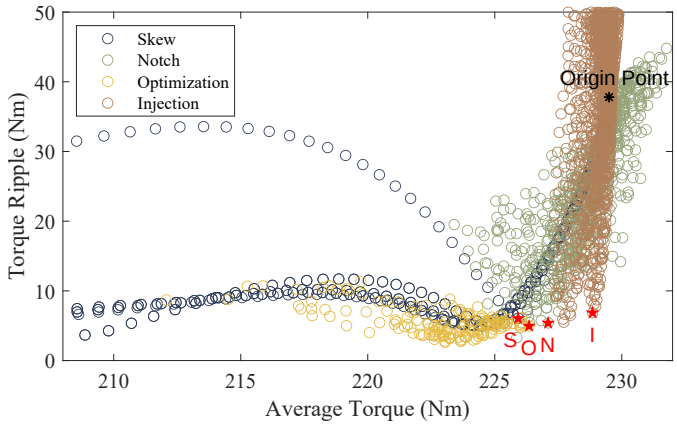

Figure 7.7: Comparison between design-oriented method and harmonics injection method

7.3 Stochastic Gradient Descent Method

7.3.1 Harmonics Decomposition

The previous analysis validates the effectiveness of the HCI method, however, it consumes plenty of time to find the amplitude and phase of injected current using parametric sweeps. Besides, harmonic injection to the three phase system will increase the complexity of control system. Therefore, the proposed method focuses on the injection into d-q system, and find the amplitude and phase automatically.

In order to inject harmonics, the harmonics should be decomposed and extracted from the signal. The fundamental and harmonic components can be expressed as

$$\boldsymbol{u} = \boldsymbol{u_1} + \boldsymbol{u_n} = \sum_{k=1}^{n} (a_k cos(k\omega_0 t) + b_k sin(k\omega_0 t)) \tag{7.4}$$

The fundamental current components can be expressed as a residual signal, which is the difference between input current and harmonic current components

$$\boldsymbol{u_1} = \boldsymbol{u} - \boldsymbol{u_n} = \boldsymbol{b} - \boldsymbol{Ax} = y(n) - x(n) = e(n) \tag{7.5}$$

7.3.2 Algorithm

In (7.5), the amplitude and phase of the harmonic components are unknown. Therefore, to track specific order harmonic components, the initial estimated harmonic current can be set as the reference frequency signal multiplied by the weighting coefficients

$$\boldsymbol{u_n} = \sum_{k=1}^{n} \boldsymbol{Ax} = \sum \boldsymbol{r_n w_n} \tag{7.6}$$

The reference harmonics matrix $\boldsymbol{r_n}$ can be expressed as

$$\boldsymbol{r_n} = \begin{bmatrix} cos_n(k\omega_e t) & sin_n(k\omega_e t) \end{bmatrix} = \boldsymbol{A} \tag{7.7}$$

where k is the harmonic order.

The weighting coefficients w^n which need be tuned to fit the optimal values, can be expressed as

$$\boldsymbol{w_n} = \begin{bmatrix} w_n^{cos} & w_n^{sin} \end{bmatrix}^T = \boldsymbol{x} \tag{7.8}$$

The desired fundamental component can be expressed as the difference between total current and harmonic current components.

$$\boldsymbol{\Lambda_n} = \boldsymbol{u} - \boldsymbol{r_n w_n} = \boldsymbol{b} - \boldsymbol{Ax} = e(n) \tag{7.9}$$

When the machine operates at steady state, the fundamental components will be the same. At this instant, when (7.9) converge to the minimum value, the estimated harmonic components in (7.6) reach the maximum value. Then, the estimated harmonic components can be considered as the extracted components.

Based on this concept, the harmonics decomposition is transformed to an optimization problem. Hence, the stochastic gradient descent method is applied to this process.

The cost function is selected as follow,

$$\min_x f(x) = \frac{1}{2} \|\boldsymbol{b} - \boldsymbol{Ax}\|^2 \tag{7.10}$$

and the gradient of the cost function can be expressed as,

$$\nabla f(x) = -\boldsymbol{A}^T(\boldsymbol{b} - \boldsymbol{Ax}) = -\boldsymbol{A}^T \boldsymbol{\Lambda} \tag{7.11}$$

Since stepping in the direction of the gradient represents maximizing the cost function[27], to get the minimum value of (7.10), the gradient descent method will iteratively update towards the opposite direction of the gradient, as follows

$$\begin{aligned} \boldsymbol{x}(k+1) &= \boldsymbol{x}(k) - \eta \nabla f(x) \\ &= \boldsymbol{x}(k) + \eta \boldsymbol{\Lambda} \begin{bmatrix} cos_n(k\omega_e t) \\ sin_n(k\omega_e t) \end{bmatrix} \end{aligned} \tag{7.12}$$

where η is the learning rate.

The stochastic gradient descent process is illustrated in Fig. 7.8.

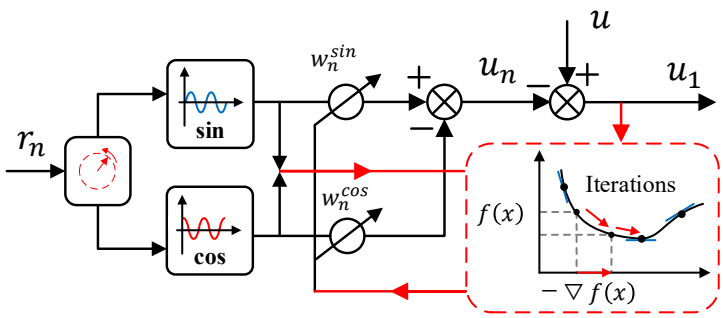

Figure 7.8: Block diagram of stochastic gradient descent method

7.3.3 Phase-Locked Loop

To identify the phase of harmonic components, a phase-locked loop (PLL) is utilized in this section. PLL can synchronize the phase and frequency of an output signal with a reference signal. The basic configuration of a PLL is shown in Fig. 7.9, and it contains three parts, phase detector (PD), loop filter (LF) and voltage-controlled oscillator (VCO).

The PD compares the phase of the input and output signals and produces an error signal based on the difference between the phases. The LF can reduce the noise and stabilizes the system. The VCO adjusts its frequency accordingly and generates the output signal. The whole loop will repeat its operation until the signals are synchronized.

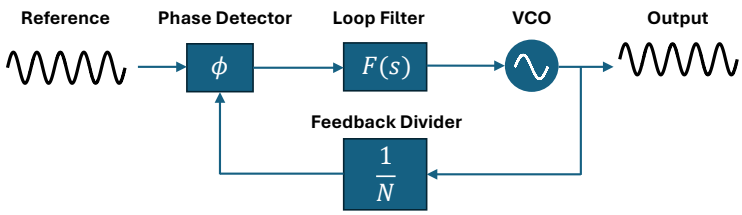

Figure 7.9: Block diagram of the Phase Locked Loop

7.3.4 Results

Torque Ripple Decomposition

To verify the proposed method, MATLAB/Simulink is utilized to implement the algorithm. The ROM of reference PMSM is extracted by JMAG-RT, and fed by ideal sinusoidal current.

The extracted torque ripple are shown in Fig. 7.10. It can be seen that the amplitude of extracted torque ripple matches with the FFT analysis in Fig. 6.5b. It means that, with the PLL, the proposed method can detect the phase of torque ripple, and further estimate the amplitude to decompose the torque ripple. Based on the extracted torque ripple, the overall torque ripple reduction is shown in Fig. 7.11.

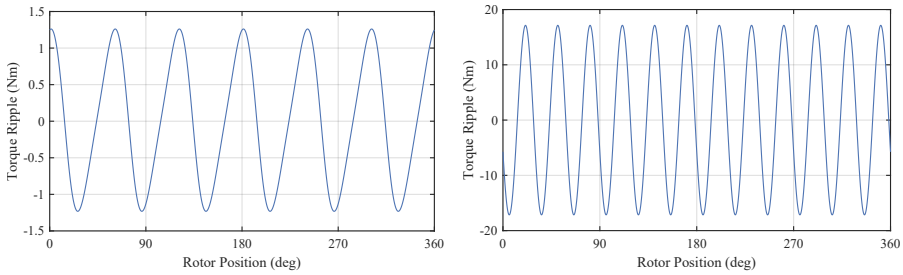

(a) 6th torque ripple decomposition

(b) 12th torque ripple decomposition

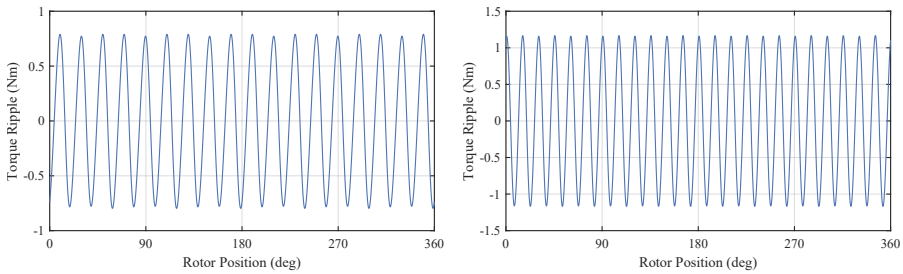

(c) 18th torque ripple decomposition

(d) 24th torque ripple decomposition

Figure 7.10: Torque ripple decomposition with the stochastic gradient descent method

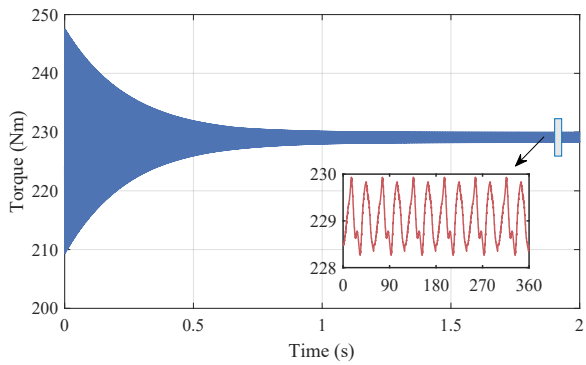

Figure 7.11: Torque ripple reduction with the stochastic gradient descent method

Degree of Freedom

In (7.8), the number of weighting coefficients N is the degree of freedom. Changing DOF of the SGD method trades off coupled quantities including approximation capability, convergence speed, stability bound on the step size, and steady-state excess error. Correct selection of DOFs can lead to quick and accurate tuning to fit the reference signals.

Figs. 7.12 - 7.15 compare the estimation value with 4-DOF and 16-DOF using same learning rate. It can be seen that the extracted torque ripple has a faster converging time with higher DOFs. When the 16-DOF starts learning, it has 16 independent directions it can adjust simultaneously. Part of those directions correspond to strong eigen-directions of the input, and they can be estimated quickly. 4-DOF has only four directions, and each one carries more of the computing burden and consumes more time in weight space to reach the correct value. Therefore, learning rate should be modified depend on the number of DOFs. Otherwise, the mismatch between DOFs and learning rate will reduce the stability or increase the computing burden on the whole system.

Additionally, in Figs. 7.12 - 7.15, after reaching the estimated value, the weighting coefficients of 16-DOF start to drift, while the weighting coefficients of 4-DOF remain stable. It can be explained by over-parameterization, which means that the extra 12 DOFs form a redundant subspace. The extra weight vector can drift along this subspace without affecting output estimation, because the drift in these directions is not excited by the input and therefore not corrected by the gradient.

Faster transient response is achieved at the cost of weight drift and reduced stability margin. Hence, the selection of DOF should match the harmonic content actually present in the disturbance rather than being oversized for safety.

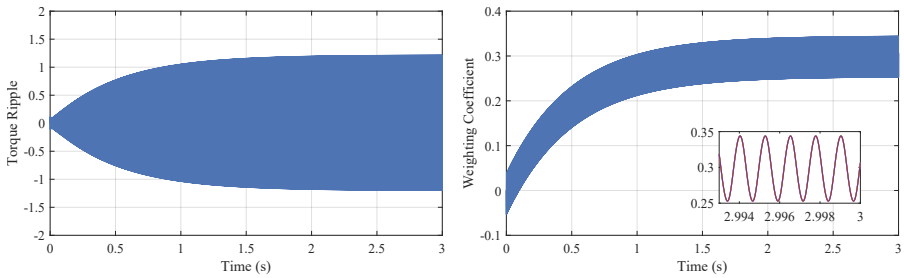

(a) 4-DOF

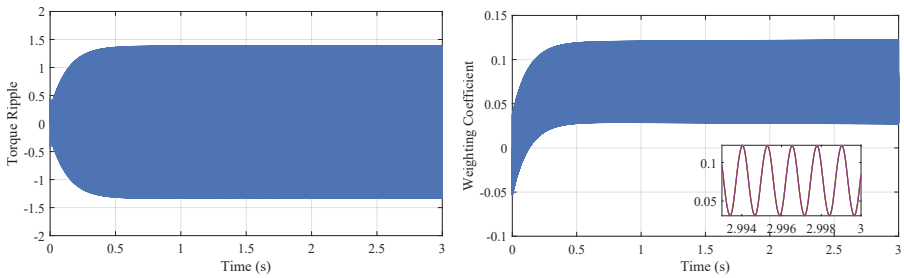

(b) 16-DOF

Figure 7.12: 6th torque ripple and weighting coefficients with 4DOF and 16DOF

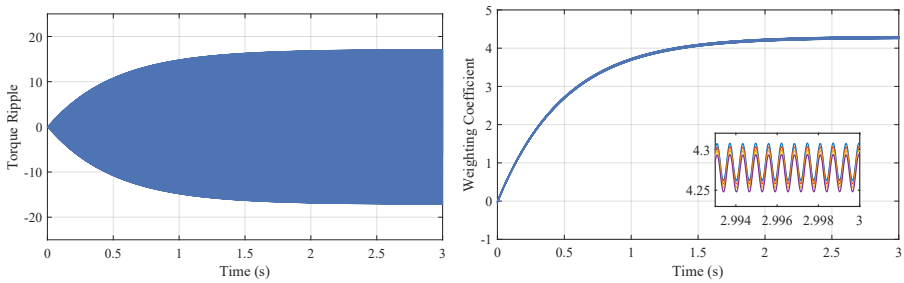

(a) 4-DOF

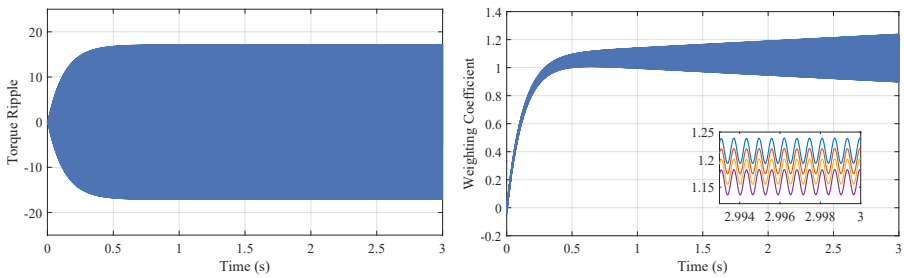

(b) 16-DOF

Figure 7.13: 12th torque ripple and weighting coefficients with 4DOF and 16DOF

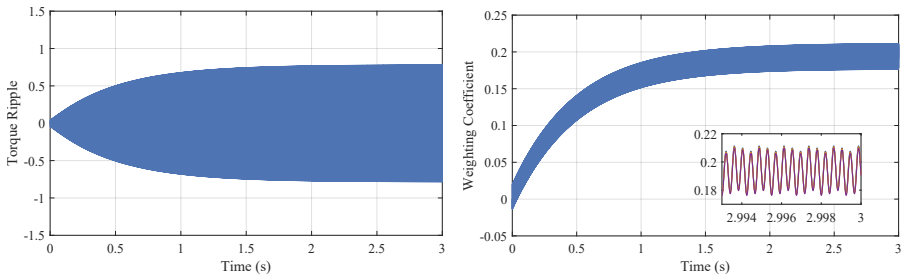

(a) 4-DOF

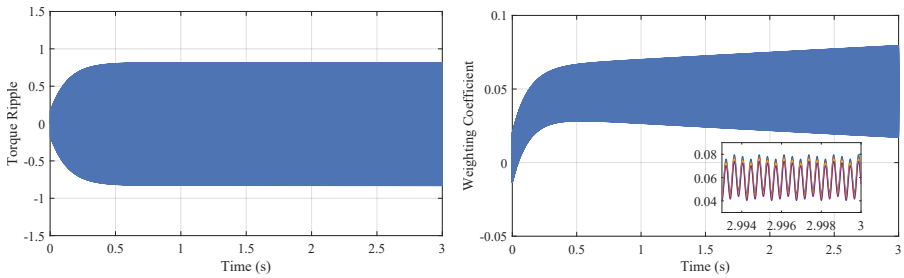

(b) 16-DOF

Figure 7.14: 18th torque ripple and weighting coefficients with 4DOF and 16DOF

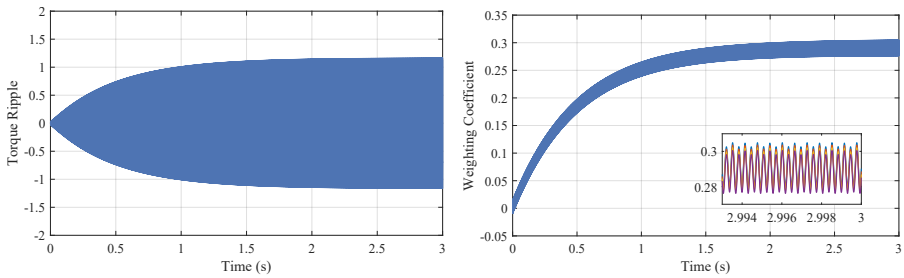

(a) 4-DOF

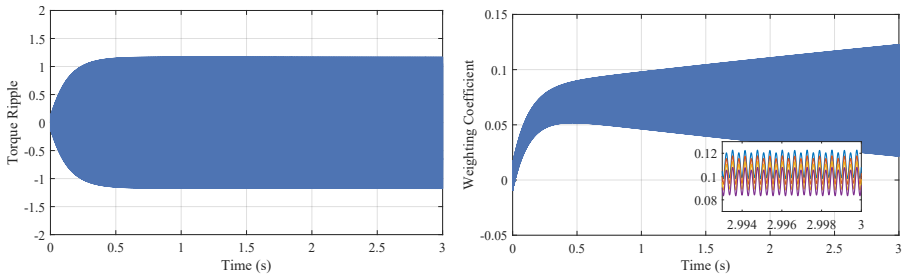

(b) 16-DOF

Figure 7.15: 24th torque ripple and weighting coefficients with 4DOF and 16DOF

7.3.5 Further Investigation

To further investigate the proposed method, the ROM of reference PMSM is fed by sinusoidal PWM with 10 kHZ switch frequency and $2\mu s$ blanking time.

The harmonic order in the proposed method is set as 5th, 7th, 11th, 13th, 17th, 19th, which are corresponding to the 6th, 12th, and 18th torque ripple. Fig. 7.16 compares the phase current, the waveform of proposed method is more sinusoidal compared to the reference. The FFT analysis of current verifies the results as well in Fig. 7.17.

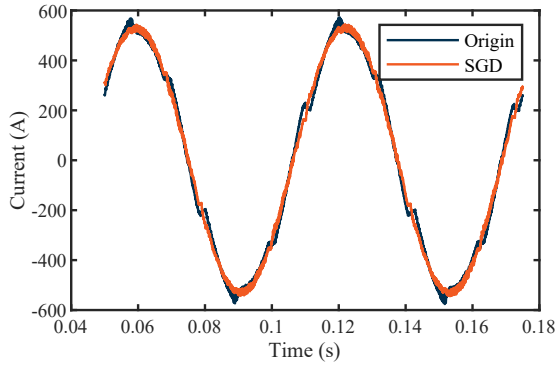

Figure 7.16: Current waveform of proposed method

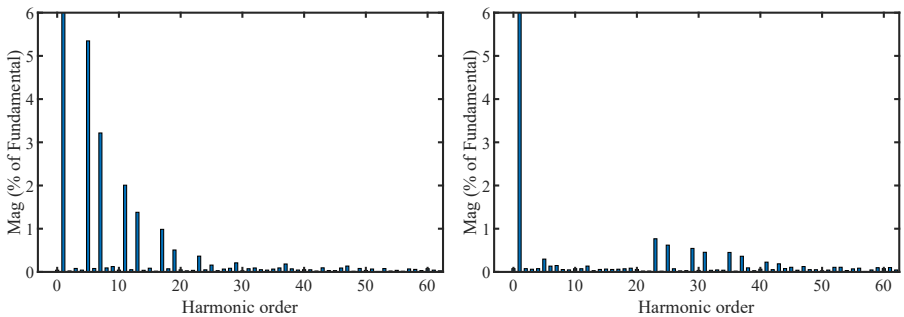

(a) Origin case **(b)** Proposed method

Figure 7.17: Current FFT between the origin case and proposed method

The result of torque ripple mitigation is shown in Fig. 7.18. It can be seen that the proposed method can significantly reduce torque ripple while maintaining average torque. The FFT analysis of torque is shown in Fig. 7.19, it can be seen that the 6th, 12th and 18th torque harmonics are significantly reduced.

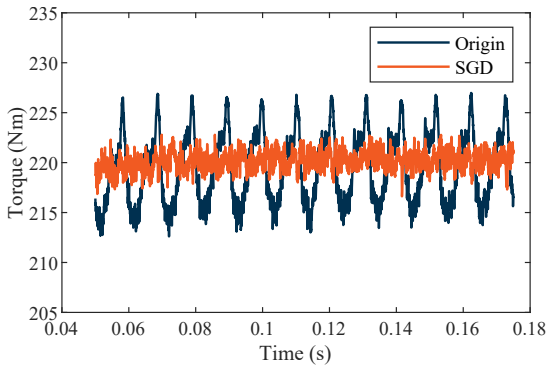

Figure 7.18: Torque waveformof proposed method

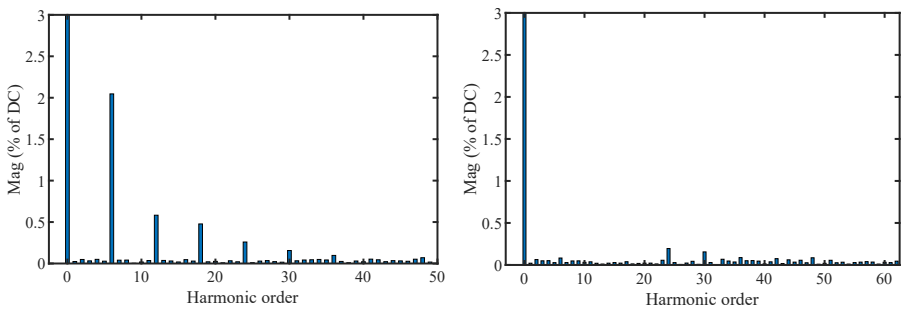

(a) Origin case **(b)** Proposed method

Figure 7.19: Torque FFT between the origin case and proposed method

CHAPTER 8

Conclusion and Future Work

8.1 Conclusion

This study presents and investigates a workflow regarding the PMSMs that spans from FEM modeling to circuit-based modeling, and ultimately to torque ripple mitigation.

In order to select a suitable FEM software to model a PMSM, a novel design and analysis process utilizing different commercial software with parallel tracks has been implemented to compare the procedures and to investigate any discrepancies between these software. FEM analysis was performed using a 50 kW reference PMSM, and the results show good agreement between these tracks. Ansys Motor-CAD is suitable in the initial stage of a design for its fast solving speed and various evaluation tools, however, it has discrepancies in flux linkage in some cases compared to JMAG Designer and Ansys Maxwell. For detailed analysis stage, JMAG Designer gives the best performance among these software regarding the solving time.

After the modelling PMSM in FEM software, a circuit-based model is developed to avoid time-consuming simulation when coupled with the PWM excitation. In this study, a time-efficient spatial harmonics modelling method

of a PMSM in polar coordinates is proposed. The proposed method shows high fidelity by predicting the saturation and spatial harmonics effects of the PMSM. The results show a good agreement with FEM simulation results, regarding the current, torque, flux and core loss. Compared to the model in the Cartesian coordinates, the proposed model significantly reduce the FEM solving cases by 21.4% and solving time by 45.5%. Besides, the nonlinear increase mapping time of PMSM model in JMAG is also discussed.

Moving towards torque ripple mitigation, this study investigates widely used design-oriented mitigation methods, including skewing, notching, and topology optimization. Furthermore, the optimal design parameters of these methods are discussed. The results show that the design-oriented methods can reduce the torque ripple by 86.2%, 91.2% and 93.1%, respectively. Taking the aforementioned analysis as a reference, a control-oriented torque ripple mitigation method based on the stochastic gradient descent algorithm is proposed. To implement the proposed method, the ROM of the reference PMSM with PWM excitation was utilized. Compared to the conventional design-oriented approaches, the proposed method can effectively mitigate torque ripple without any design modification. Besides, the DOF of weighting coefficients in the proposed method is also discussed in terms of the converging time.

Overall, this study reveals the potential of the HCI method, which is competitive with the design-oriented method but without hardware modification.

8.2 Future Work

This study presented some preliminaries and primary investigations of torque ripple and NVH reduction. However, there are many aspects of current study that need to be improved.

Therefore, future work can be listed as follows

- Implement the experimental validation of the proposed method, which will provide deep and insightful knowledge about the physical phenomena of torque ripple and NVH.

- Investigate the possibility of reducing the computational burden. The adaptive method requires high computational resources, and it is necessary to develop an efficient mitigation method.

- Determine the overall losses of the HCI method compared to other mitigation methods. And find the possibilities to optimize the losses.
- Investigate the sideband vibration and other PWM induced torque ripple.

References

[1] C. A. Lopez, W. R. Jensen, S. Hayslett, S. N. Foster, and E. G. Strangas, "A review of control methods for pmsm torque ripple reduction," in *2018 XIII International Conference on Electrical Machines (ICEM)*, 2018, pp. 521–526.

[2] M. Toren and M. Çelebi, "A comparison of the programmes using finite element software in electrical machine design," *International Journal of Applied Mathematics Electronics and Computers*, no. Special Issue-1, pp. 391–398, 2016.

[3] M. Zaheer, P. Lindh, L. Aarniovuori, and J. Pyrhönen, "Assessment of 5 kW induction motor finite element computations with a commercial and an open-source software," in *2019 International Aegean Conference on Electrical Machines and Power Electronics (ACEMP) & 2019 International Conference on Optimization of Electrical and Electronic Equipment (OPTIM)*, 2019, pp. 114–119.

[4] M. TZaheer, P. Lindh, L. Aarniovuori, and J. Pyrhönen, "Comparison of commercial and open-source FEM software: A case study," *IEEE Transactions on Industry Applications*, vol. 56, no. 6, pp. 6411–6419, 2020.

[5] C. Di, X. Bao, J. Pan, and C. Wang, "Modelling and analysis of a ferrite assisted synchronous reluctance machine based on the open-source platform elmer," *Transactions of China Electrotechnical Society*, vol. 37, no. 5, pp. 1136–1144, 2022.

[6] R. Marţiş, F. P. Pîgleşan, C. Marţiş, L. Szabo, and M. Ruba, "Design and optimization platform for synchronous motors," in *2018 International Symposium on Power Electronics, Electrical Drives, Automation and Motion (SPEEDAM)*, 2018, pp. 314–318.

[7] X. Chen, J. Wang, B. Sen, P. Lazari, and T. Sun, "A High-Fidelity and Computationally Efficient Model for Interior Permanent-Magnet Machines Considering the Magnetic Saturation, Spatial Harmonics, and Iron Loss Effect," *IEEE Transactions on Industrial Electronics*, vol. 62, no. 7, pp. 4044–4055, 2015.

[8] L. Quéval and H. Ohsaki, "Nonlinear abc-Model for Electrical Machines Using N-D Lookup Tables," *IEEE Transactions on Energy Conversion*, vol. 30, no. 1, pp. 316–322, 2015.

[9] M. Pizzuto, A. Balamurali, H. Mohammadi, and N. C. Kar, "Impact of Model Fidelity on Control and Performance Analysis of Interior Permanent Magnet Synchronous Machines," in *2024 International Conference on Electrical Machines (ICEM)*, 2024, pp. 1–6.

[10] H. Cai and D. Hu, "On PMSM Model Fidelity and its Implementation in Simulation," in *2018 IEEE Energy Conversion Congress and Exposition (ECCE)*, 2018, pp. 1674–1681.

[11] S. Agoro and I. Husain, "High-fidelity nonlinear modeling of an asymmetrical dual three-phase pmsm," in *2023 IEEE International Electric Machines Drives Conference (IEMDC)*, 2023, pp. 1–7.

[12] D. Hu, Y. M. Alsmadi, and L. Xu, "High-Fidelity Nonlinear IPM Modeling Based on Measured Stator Winding Flux Linkage," *IEEE Transactions on Industry Applications*, vol. 51, no. 4, pp. 3012–3019, 2015.

[13] S. Li, D. Han, and B. Sarlioglu, "Modeling of Interior Permanent Magnet Machine Considering Saturation, Cross Coupling, Spatial Harmonics, and Temperature Effects," *IEEE Transactions on Transportation Electrification*, vol. 3, no. 3, pp. 682–693, 2017.

[14] M. S. Rafaq, W. Midgley, and T. Steffen, "A review of the state of the art of torque ripple minimization techniques for permanent magnet synchronous motors," *IEEE Transactions on Industrial Informatics*, vol. 20, no. 1, pp. 1019–1031, 2024.

[15] J. Du et al., "Multiple harmonics suppression of back emf in pmsms by an improved magnet-skewing method," *IEEE Transactions on Transportation Electrification*, vol. 11, no. 5, pp. 10 977–10 987, 2025.

[16] Z. S. Du and T. A. Lipo, "Reducing torque ripple using axial pole shaping in interior permanent magnet machines," *IEEE Transactions on Industry Applications*, vol. 56, no. 1, pp. 148–157, 2020.

[17] H. Ge, X. Qiu, B. Guo, J. Yang, C. Bai, and Z. Jin, "Optimized rotor shape for reducing torque ripple and electromagnetic noise," *IEEE Transactions on Magnetics*, vol. 58, no. 2, pp. 1–5, 2022.

[18] H. Chuan, S. M. Fazeli, Z. Wu, and R. Burke, "Mitigating the torque ripple in electric traction using proportional integral resonant controller," *IEEE Transactions on Vehicular Technology*, vol. 69, no. 10, pp. 10 820–10 831, 2020.

[19] M. Gu, Z. Wang, C. Zhu, and M. Cheng, "Torque ripple modeling and mitigation for pmsm by harmonic current injection based on general air-gap field modulation theory," in *IECON 2024 - 50th Annual Conference of the IEEE Industrial Electronics Society*, 2024, pp. 1–6.

[20] J. Pyrhonen, T. Jokinen, and V. Hrabovcova, *Design of Rotating Electrical Machines*. John Wiley & Sons, Ltd, 2013.

[21] W. Liang, P. C.-K. Luk, and W. Fei, "Analytical investigation of sideband electromagnetic vibration in integral-slot pmsm drive with svpwm technique," *IEEE Transactions on Power Electronics*, vol. 32, no. 6, pp. 4785–4795, 2017.

[22] R. Tsunata and M. Takemoto, "Skewing technology for permanent magnet synchronous motors: A comprehensive review and recent trends," *IEEE Open Journal of the Industrial Electronics Society*, vol. 5, pp. 1251–1273, 2024.

[23] G. Lei, T. Wang, J. Zhu, Y. Guo, and S. Wang, "System-level design optimization method for electrical drive systems—robust approach," *IEEE Transactions on Industrial Electronics*, vol. 62, no. 8, pp. 4702–4713, 2015.

[24] C. Xia, B. Ji, and Y. Yan, "Smooth speed control for low-speed high-torque permanent-magnet synchronous motor using proportional integral resonant controller," *IEEE Transactions on Industrial Electronics*, vol. 62, no. 4, pp. 2123–2134, 2015.

[25] X. Shi, Y. Le Menach, J.-P. Ducreux, and F. Piriou, "Comparison of slip surface and moving band techniques for modelling movement in 3d with FEM," *COMPEL-The international journal for computation and mathematics in electrical and electronic engineering*, vol. 25, no. 1, pp. 17–30, 2006.

[26] E. Jansson, T. Thiringer, and E. Grunditz, "Time resolution dependency of core loss accuracy in finite element analysis of a permanent magnet synchronous machine," in *2020 International Conference on Electrical Machines (ICEM)*, vol. 1, 2020, pp. 1011–1017.

[27] S. Ruder, *An overview of gradient descent optimization algorithms*, 2017.